



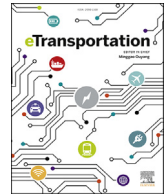
Thermal capability of electric vehicle PMSM with different slot areas via thermal network analysis

Downloaded from: <https://research.chalmers.se>, 2024-04-19 00:59 UTC

Citation for the original published paper (version of record):

Grunditz, E., Thiringer, T., Lindström, J. et al (2021). Thermal capability of electric vehicle PMSM with different slot areas via thermal network analysis. *eTransportation*, 8. <http://dx.doi.org/10.1016/j.etrans.2021.100107>

N.B. When citing this work, cite the original published paper.



Thermal capability of electric vehicle PMSM with different slot areas via thermal network analysis

Emma Arfa Grunditz^{a,*}, Torbjörn Thiringer^a, Joachim Lindström^b,
Sonja Tidblad Lundmark^a, Mikael Alatalo^a

^a Chalmers University of Technology, Göteborg, Sweden

^b Volvo Cars, Göteborg, Sweden

ARTICLE INFO

Article history:

Received 11 September 2020

Received in revised form

23 December 2020

Accepted 10 January 2021

Keywords:

Electric machine

Electric vehicle

Energy consumption

Lumped parameter thermal network

Thermal modelling

ABSTRACT

In this paper, the effect that a varied stator slot size has on the efficiency and thermal capability of a permanent magnet synchronous machine for an electric vehicle, is evaluated and quantified. A machine with four differently sized slot areas was electromagnetically evaluated with finite element analysis, and thermally with a lumped parameter network model. By decreasing the slot size while keeping other dimensions fixed, the core losses reduce due to the wider magnetic path, whereas the winding losses increase. Additionally, a higher maximum torque is reached due to reduced saturation. Results are compared in the machine's torque-speed operating area regarding machine-part and total losses, continuous torque and transient overload capability, as well as during 19 low, middle and high-speed drive cycles regarding energy losses and peak winding temperature. The largest slot showed the lowest winding losses and thus the highest thermally limited torque capability. In contrast, the energy losses with the largest slot were the highest in 13 of the drive cycles, and the lowest in 11 of them with the smallest slot due to its lower part load (i.e. core) losses. The smallest slot would also result in the lowest material cost since it has the least copper.

© 2021 The Author(s). Published by Elsevier B.V. This is an open access article under the CC BY-NC-ND license (<http://creativecommons.org/licenses/by-nc-nd/4.0/>).

1. Introduction

An electric machine's torque and power rating is largely limited by a high winding temperature which degrades the insulation and shorten the machine's lifetime. In case of permanent magnet machines, additionally, high magnet temperatures increase the risk of demagnetization [1,2].

Common design targets for propulsion electric machines are high performance and efficiency, as well as low weight, volume and cost. Typically, machines in electric vehicles (EVs) experience highly dynamic load cycles, which cause similarly varying internal losses, and therefore strongly time dependent temperature fluctuations. As a trade-off, machines are generally designed to handle a certain time of overload before reaching a critical winding temperature. Therefore, apart from electromagnetic and mechanical

evaluation, it is vital to also consider thermal aspects during the design process of propulsion machines. The interest to do so has increased lately partly due to the expanded interest in transport electrification.

It is generally assumed that for machine modelling and simulation, the most accurate results are achieved using well representative computer aided design (CAD) models and numerical solvers. However, the computation effort providing sufficient data for evaluation is substantial, especially for conjugate heat transfer analysis including fluid dynamics. Therefore, producing useful characterization over the whole operating region, as is needed during drive cycle evaluations for vehicles, reduced order thermal models such as lumped parameter networks (LPN) are readily used [1,3].

A popular electromagnetic machine design process is to use multi-objective optimization methods, where both geometrical and material parameters are varied in order to comply with requirement targets such as high torque, low losses, torque ripple, and material cost [4,5]. To achieve these targets, thermal LPN modelling and evaluation are preferably included in the optimization loop [6,7], or it can be applied on the resulting optimized design, or a few selected design options for comparison [8–10].

* Corresponding author.

E-mail addresses: emma.grunditz@chalmers.se (E.A. Grunditz), torbjorn.thiringer@chalmers.se (T. Thiringer), joachim.lindstrom@volvocars.se (J. Lindström), sonja.lundmark@chalmers.se (S. Tidblad Lundmark), alatalo@chalmers.se (M. Alatalo).

Alternatively, the design analysis can focus on a single design aspect such as the pole/slot combination [11], the shape of the slot [12], or on external factors such as the gear ratio [13], all while using thermal LPN models to evaluate temperature. Another option is to perform several consecutive single design parameter sweeps as in Ref. [14].

Often the proposed optimized designs are electromagnetically and thermally evaluated over one or two drive cycles, as in Refs. [10,11,13]. Occasionally a few more drive cycles are utilized as in Ref. [4] where five cycles are used as a combined weighted input to the optimization.

In short, many papers have been published that suggest valuable modelling and simulation techniques as well as optimization procedures, applied to electric machines in electric vehicles that take thermal aspects into consideration.

To further build on the concept of focused design studies, the purpose of this paper is to evaluate the effect that a varied stator slot size has on the electromagnetic efficiency and thermal capability of a permanent magnet synchronous machine (PMSM) for a light-duty (passenger car) battery electric vehicle (BEV). The electromagnetic losses are evaluated using finite element analysis (FEA) and the temperatures are evaluated using a thermal lumped parameter model, with temperature adjusted losses as input.

It is then anticipated that a larger slot area will lead to reduced winding losses and increased core losses due to a thinner magnetic path. Hence, by varying the slot size, losses can be shifted between the winding and the core.

The specific aim of this paper is to quantify and compare some selected properties for four different slot sizes (named Original, Small, Large, High):

- loss-distribution in the torque-speed-plane
- thermal steady state maximum torque (i.e. continuous torque) as a function of speed for a chosen critical winding temperature
- maximum intermittent torque for fixed maximum rms current
- transient overload capability in terms of time duration at different torque-speed-operating-points before reaching a critical winding temperature
- drive cycle temperature-adjusted total losses and losses per machine part, for a wide range of different cycles
- drive cycle winding and magnet maximum temperature

Throughout the study, the outer and internal machine dimensions are fixed (except slot size), as well as the current and voltage ratings of the battery and inverter, and the mechanical ratings of the transmission. This is regarded as a justified scope, since in automotive industry, packaging is usually strictly constrained. Additionally, a variation in one component should preferably not require a change in any of the other drive system components, since that would lead to significantly increased costs.

2. Reference PMSMs

The reference machine is a permanent magnet synchronous machine (PMSM), since this type is very common in today's battery electric vehicles (BEVs) [15]. They provide high torque and power densities, along with a high efficiency.

The lamination cross section is similar to commercially popular designs [16], especially the Toyota Prius 2004 motor, with 48 slots, 8 poles, v-shaped interior permanent magnet (IPM) configuration, with a distributed winding in 2-layers, as shown in Fig. 1. However, the stator teeth and yoke are thinner and a different angle for the v-shaped magnet arrangement is used, compared to Prius 2004. A simplified frame with a spiral liquid cooling channel (shown in Fig. 12) and shaft with two ball bearings are also presented in Fig. 1.

A reference machine (with the Original slot size) is sized to fulfil the specified requirements of a conceptualized large size battery electric vehicle (BEV), as presented in Table D12. The sizing procedure is further described in Ref. [17]. Selected data for this machine is shown in Table 1.

Based on the reference machine, four different slot areas are investigated: Small, Original, High and Large, as in Fig. 2. The reference machine is henceforth referred to as the machine with the Original slot. The Small slot has both wider teeth and yoke, whereas the Large slot has a bit thinner teeth and yoke, and the High slot only thinner yoke, all relative the Original slot size, as shown in Table 2. The gross copper fill factor is the same in all cases (deviates less than 1%), thus the winding cross sectional area varies with slot area, as presented in Table 2. This is based on the assumption of using conductors of various diameters within the same coil.

To minimize the effect on inverter and battery during this investigation, the maximum dc voltage is 400 V, and the maximum rms phase current is 251 A in all four cases. The latter means that the maximum current density is the largest in the Small slot and the lowest in the Large slot.

The chosen materials are listed in Table 3, and their properties presented in Table B.8 and B.9 in Appendix B. For some material data, the temperature dependence is found and thus used, as shown in Fig. B.28, B.29, B.30, B.31 and B.32 in Appendix B. Specifically, the magnet strength decreases with increasing temperature. The mass of different motor parts with Original slot machine is presented in Table 4. The Small slot machine has the least amount of copper and the largest amount of steel. Since copper is more expensive than laminations per unit mass [18], the Small slot machine material can be expected to be the cheapest of the four.

3. FEA and machine mapping

Machines with the four slot variants have been simulated, in the electromagnetic finite element analysis (FEA) software Ansys Maxwell in 2D. The simulated machine geometry and mesh density is shown in Fig. 1. For simplicity, the lamination stacking factor is ignored in all electromagnetic simulations.

For each machine geometry, at 13 different speed levels (i.e. at 1 rpm, and at every 1000 rpm up to 12,000 rpm), 11×11 operating points in the id-iq plane have been evaluated using sinusoidal current excitation for two electrical periods, with 101 sample points. The data resolution in the id-iq-plane is then increased through interpolation, as shown in Fig. 3a. From this, the Max Torque Per Ampere (MTPA) operating points as well as the field weakening operation is numerically found for each integer torque level, within the allowed operating current and voltage limits, as exemplified in Fig. 3b. A final interpolation in the speed range is then conducted.

The core losses (hysteresis and eddy) are calculated as the mean value over the second of the two electrical periods, and the magnets are modeled as zero current carrying coils while considering eddy effects. The copper losses in the active part of the winding are extracted from the FEA software, while ignoring both skin and proximity effects for simplicity. The end winding losses are then calculated based on its estimated length (as described in Appendix A), and added.

As the machine losses are used as input to the thermal calculations, the losses are separated into the different machine parts; core losses in the stator yoke, teeth, and rotor, winding losses in the active and end-winding parts, and eddy current losses in the magnets.

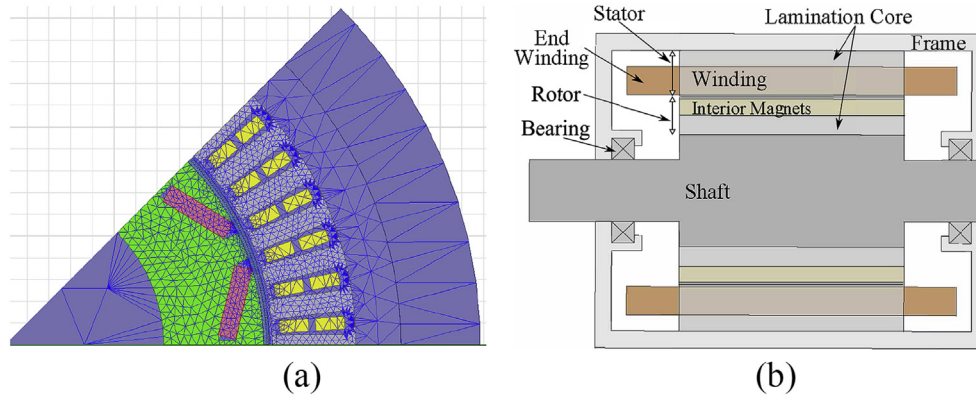


Fig. 1. One pole of the Original slot motor as entered in the FEA model, with the used mesh, as well as the axial cross section of the machine configuration. (a) Mesh. (b) Cross section.

Table 1
PMSM data with the Original slot size.

Parameter	Value, unit
Peak Power	89 kW
Max. Torque	214 Nm
Base speed	4 000 rpm
Max. speed	12,000 rpm
Max. DC voltage	400 V
Max. rms current density	20 A/mm ²
Max. rms phase current	251 A
Core length	150 mm
Core stacking factor	95%
Lamination thickness	0.3 mm
Number of slots	48
Number of poles	8
Stator outer diameter	182 mm
Stator inner diameter	122.9 mm
Stator yoke thickness	10.4 mm
Tooth width	4.5 mm
Tooth height	19.2 mm
Slot opening width	1.8 mm
Slot fill factor	45%
Turns per coil	6
Coils per pole per phase	4
Rotor outer diameter	121.5 mm
Rotor inner diameter	72.8 mm
Air gap length	0.7 mm
Magnet thickness	4.1 mm
Magnet width	16.4 mm

Table 2
Slot data and active/end-winding length ratio.

	Small	Original	Large	High
H_{slot} (%)	85%	100%	115%	115%
W_{slot} (%)	85%	100%	100%	115%
A_{slot} (mm ²)	60.96	83.74	109.66	94.30
	73%	100%	131%	113%
A_{Cu} (mm ²)	27.23	37.69	49.84	42.65
	72%	100%	132%	113%
$J_{rms,max}$ (A/mm ²)	28	20	15	18
	138%	100%	76%	88%
I_{act}/I_{tot}	54.5%	52.3%	50.2%	51.3%

Table 3
Material of machine parts, and data reference.

Part	Material	
Frame	Aluminum alloy 195	[19]
Lamination	NO30, Tata Cogent	[20]
Winding	Copper	[19]
Winding impreg.	Unsaturated polyester	[21]
Magnets	NdFeB NEOMAX NMX-37F, Hitachi	[22]
Shaft	Carbon-silicon steel	[19]

Table 4
Mass (kg) of reference (original slot) PMSM parts.

Motor Part	Original
Frame	5.5
Stator Yoke	6.0
Stator Teeth	4.9
Active winding	2.4
Slot impregnation	0.4
End Winding	2.2
Magnets	1.2
Rotor laminations	6.7
Shaft	5.8
Bearings	0.4
Total	35.5

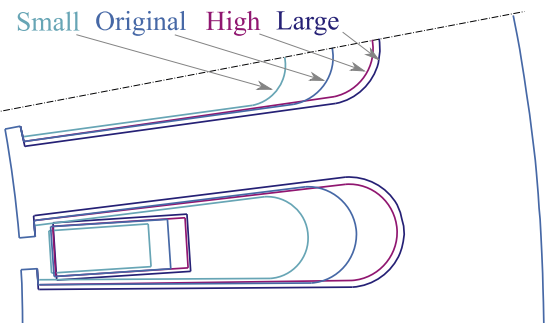


Fig. 2. The FEA simulated different stator lamination geometries, as well as one of the winding layers.

3.1. FEA results - original slot at three temperatures

With each slot size, the FEA simulations are done at the three magnet temperatures; 20 °C; 70 °C and 120 °C.

Due to the weakening of the magnet with increasing temperature, the produced maximum torque decreases with temperature.

Moreover, for the same torque in the MTPA area of operation, a larger current is needed. In contrast, in the field weakening area, the weaker magnet leads to a reduced need for field weakening current, especially at the lower torque levels. This is illustrated in Fig. 4a.

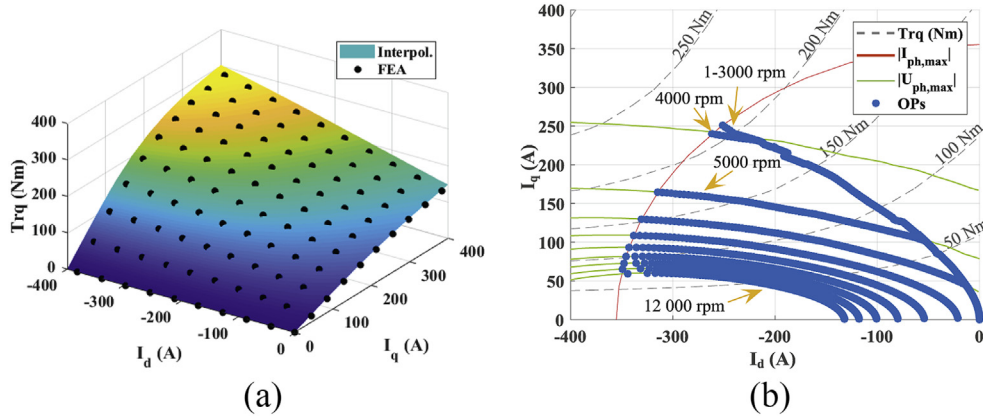


Fig. 3. FEA simulated operating points for each speed level along with resulting interpolated torque, and current control i_d i_q reference values for each integer torque level, at 1 rpm and every 1000 rpm up to max. speed. (a) FEA operating points and interpolated torque. (b) Result of current control algorithm.

The winding losses shown in Fig. 4b, depend on both current and winding resistance, which increase with temperature. The increased resistance thus somewhat counteracts the reduced current in the field weakening area at higher temperatures.

The lower field weakening current also cause minor deviations in the magnet losses in the torque-speed diagram shown in Fig. 5a. The resulting total losses for the three different temperatures are presented in Fig. 5b.

3.2. FEA results - four slot sizes

The magnet flux linkage as a function of q-axis current for each slot size, is shown in Fig. 6, at 70 °C. In general the flux linkage from the magnet decreases with increasing q-axis current due to saturation. The saturation effect is the largest for the Large slot, since its teeth and yoke are the thinnest, whereas the it is the smallest for the Small slot with the thickest teeth and yoke. The difference in produced torque between the geometries is shown in Fig. 6b to decrease with decreasing current, especially with decreasing q-axis current.

The resulting dq current operating points from the current control algorithm, are presented in Fig. 7a, for a few selected speed levels. The MTPA method result in a somewhat larger share of the q-axis current for the Small slot geometry compared to the others. As a consequence, a bit higher torque levels can be reached for the same current magnitude.

The higher flux linkage from the magnet also result in a stronger speed dependence of the induced voltage, hence the base speed is

lower for the Small slot compared to the others. In the field weakening area, instead a larger d-axis current is needed in the Small slot in order to suppress the flux from the magnet, that is even though its d-axis inductance is larger. This counteracts some of the previous torque producing advantages with the Small slot.

As a consequence, at low speed levels the largest produced torque per input rms current is given by the Small slot geometry and the lowest by the Large slot. At higher speed levels the difference is quite small. The results are shown for a few example speed levels in Fig. 7b. The resulting max. torque as a function of speed is shown as the dashed line in Fig. 8a.

The total core losses are also presented in Fig. 8a. Likely, the wider teeth and yoke for the Small slot geometry cause somewhat lower flux density levels, hence the lowest core losses. At low torque levels the core losses are the largest in the Large slot geometry, whereas at higher torque levels they are the largest in the High slot. The opposite order is noted in the rotor (although not shown here), i.e. largest for the Small slot and lowest for the Large. Still, the magnitude of the core losses in the rotor are much lower than in the stator. In almost the whole speed-torque-range the majority of the core losses occur in the teeth, as shown in Fig. 8b. As the speed increases, this share also increases. For the same operating point, then the share is generally the largest for the Small slot and the lowest for the Large slot.

As shown in Fig. 9a, the difference in phase rms current between the geometries increases with increasing torque in the MTPA operating area. There, the current is the largest for the Small slot and the lowest for the Large slot. In the field weakening area, the

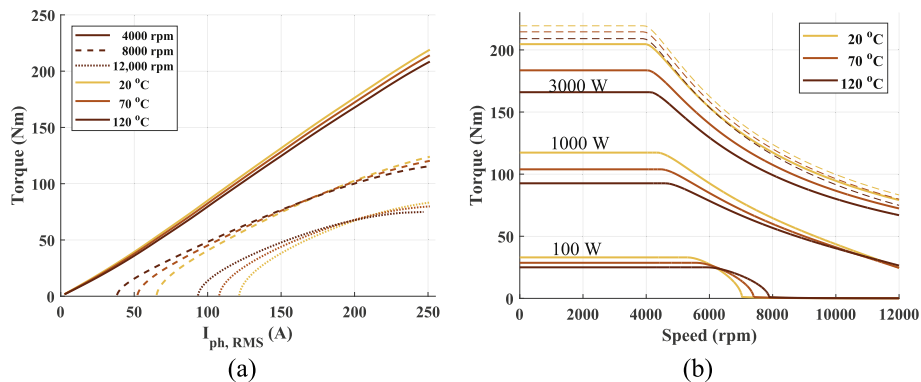


Fig. 4. Produced torque per applied rms phase current, and total winding losses as a function of torque and speed, for the Original slot motor, at winding and magnet temperature 20 °C, 70 °C and 120 °C. (a) Torque per input phase rms current. (b) Winding losses at 100 W, 1000 W and 3000 W.

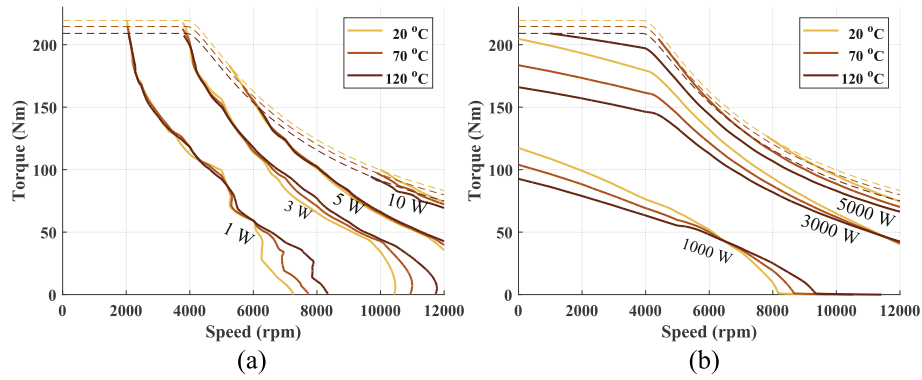


Fig. 5. Magnet and total losses as a function of torque and speed, for the Original slot motor, at winding and magnet temperature 20 °C, 70 °C and 120 °C. (a) Magnet losses at 1 W, 3 W, 5 W, and 10 W. (b) Total losses at 1 kW, 3 kW and 5 kW.

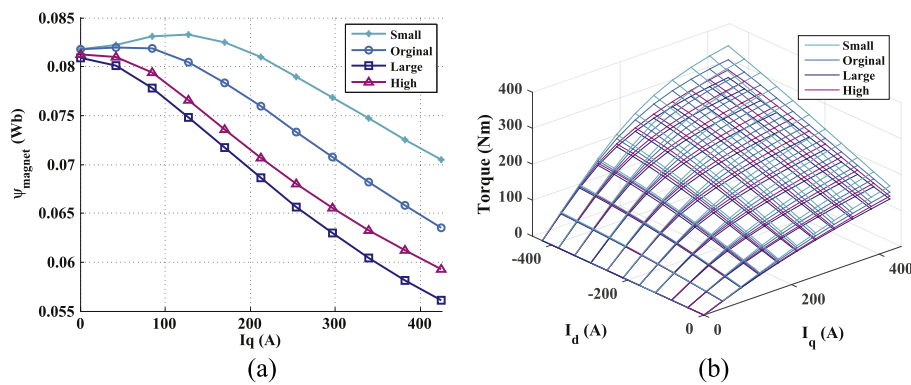


Fig. 6. Flux linkage from magnets as a function of q-axis current, and produced torque, for the different stator slot areas at 70 °C copper and magnet temperature. (a) Flux linkage from magnets (Wb). (b) Produced torque.

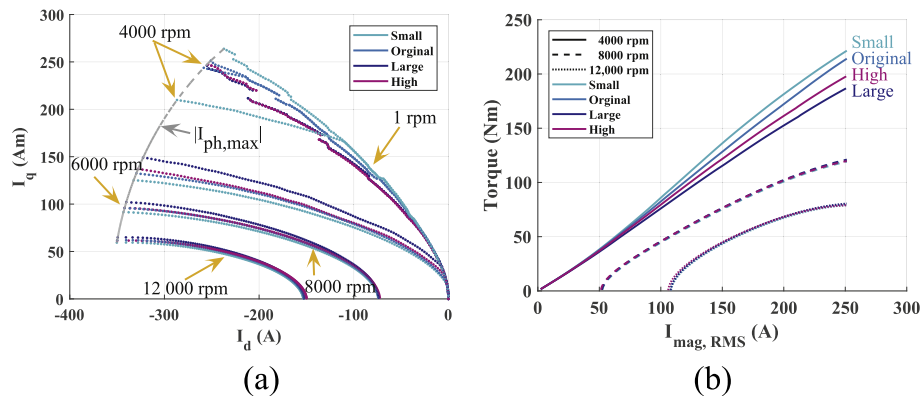


Fig. 7. Result of current control algorithm as a function of dq current, and produced torque per input rms phase current, for the different stator geometries at 70 °C copper and magnet temperature. (a) Current control. (b) Torque per input current.

current is essentially the same with all slots.

In the same time, the phase resistance is largest for the Small slot and the lowest for the Large slot, due to their different copper cross section areas. Therefore, the total copper losses, as shown in Fig. 9b, are the highest in the small slot and the lowest for the Large slot.

Nevertheless, it is only the losses with the Small slot that deviates notably in a large part of the operating area as being somewhat higher compared to the other slot geometries, as shown in Fig. 10a.

The main difference between the losses in the motors with

different slot geometries is thus not the total amount of losses, but the relation between copper and core losses, as shown in Fig. 10. As copper and core losses are the two main loss components, the rest of the losses in the figure adhere to the core losses. Consequently, core losses can be expected to dominate in drive cycles with low acceleration levels and relatively high speed levels, whereas copper losses can be expected to dominate in drive cycles with higher acceleration levels. The motor with the Small slot have a larger share of copper losses and a lower share of core losses, whereas the motors with the Large and High slots have instead a larger share of core losses and a lower share of copper losses.

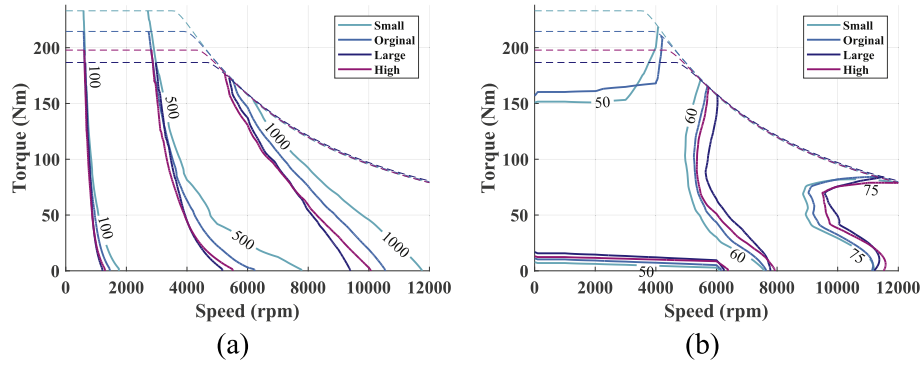


Fig. 8. Total core losses, and share of teeth losses to total core losses, both as a function of torque and speed, for the Small, Original, Large and High slot areas. (a) Total lamination core losses at 100 W, 500 W and 1000 W. (b) Share of teeth losses in % of total core losses.

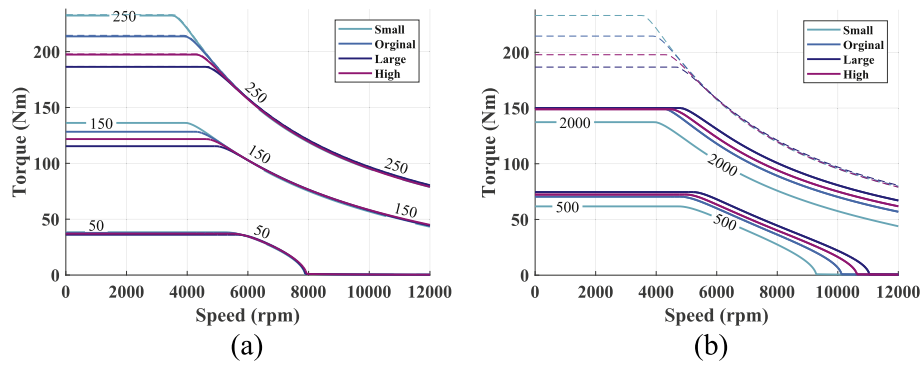


Fig. 9. RMS phase current and total copper losses, as a function of torque and speed, for the Small, Original, Large and High slot areas. (a) RMS current. (b) Copper losses at 500 W and 2000 W.

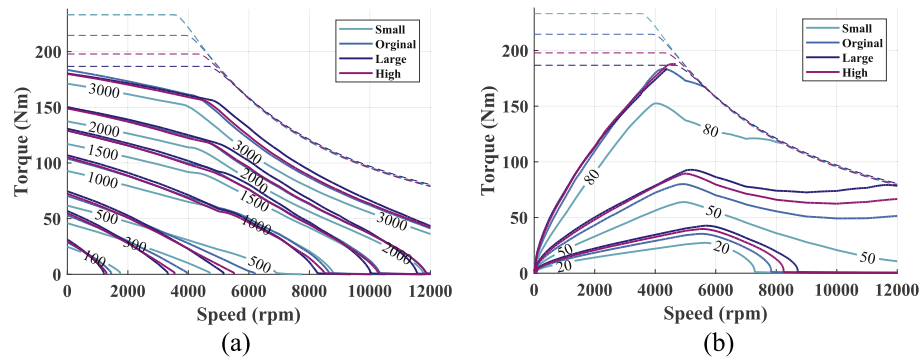


Fig. 10. Total machine losses, as well as share of copper losses to total, both as a function of torque and speed, for the Small, Original, Large and High slot areas. (a) Total losses in W. (b) Share of copper losses in % of total losses.

The phase resistance, and max. torque for all slots at the three magnet and copper temperatures are given in Table 5.

4. Thermal LPN modeling

A wide range of suggested thermal networks can be found in literature with varying complexity and node configurations. However, since the object under consideration here is a concept machine where only the active parts are geometrically determined with a high accuracy, the level of complexity of the implemented network is adjusted accordingly.

A 10-node network for TEFC IMs (totally enclosed fan cooled induction machines) is proposed in Ref. [1], where a T-equivalent

Table 5

Parameters for the four stator slot sizes.

	Small	Original	Large	High
$R_s @ 20^\circ\text{C}$ (m Ω)	24.5	18.4	14	16.6
$R_s @ 70^\circ\text{C}$ (m Ω)	29.2	22.0	17.3	19.8
$R_s @ 120^\circ\text{C}$ (m Ω)	33.9	25.5	20.1	23.0
	(133%)	(100%)	(79%)	(90%)
$T_{max} @ 20^\circ\text{C}$ (Nm)	238	219	191	203
$T_{max} @ 70^\circ\text{C}$ (Nm)	233	215	187	198
$T_{max} @ 120^\circ\text{C}$ (Nm)	227	209	181	192
	(109%)	(100%)	(87%)	(92%)

node configuration is implemented. It assumes a uniform frame

temperature, includes both radial and axial heat transfer in laminations and winding, as well as a speed dependent air gap convection and fan speed dependent convection in the end cap region. A similar fan cooled IM 8-node network is presented in Ref. [23], however without the T-equivalent node configuration. Furthermore, the axial heat transfer in the laminations are considered negligible, whereas bearing heat transfer is added. This network was later adjusted to a water cooled inset PMSM presented in Ref. [21], by mainly modifying the rotor modelling. In this paper, the network has been further adjusted for the used IPM rotor design. It is presented in Fig. 11. Similar adjustments to the rotor parts are also reported in Refs. [24–26]. Another modification here, is the added consideration of convection heat transfer to the coolant.

It is assumed that the internal heat generation is uniformly distributed in each region, as in Refs. [27–29]. Axial heat transfer is considered in the copper windings and the shaft, whereas only radial heat transfer is considered for the laminations and magnets, as in Ref. [27]. Moreover, axial symmetry around the midpoint is assumed, as well as cylindrical symmetry both geometrically and thermally. Heat transfer due to radiation is neglected.

4.1. Frame and cooling

The machines are liquid cooled, as recommended in [30, p.90] for the used current densities. The coolant is a mixture of 48% (by volume) water and 52% mono ethylene glycol [31], since 50/50 Water Ethylene Glycol (WEG) is commonly used in BEVs [15]. The temperature dependence of its material parameters are shown in Fig. 32 in Appendix B.

The thermal resistance between the coolant and the frame node $R_{th,Co-Fr}$ is the sum of the resistances for the two main heat transfer modes involved: convection between the coolant medium and the cooling duct walls, and conduction inside the frame. Both natural convection to the ambient air and any kind of radiation are considered negligible compared to the forced convection [3].

The cooling channel is formed as a spiral of four laps inside the aluminum frame, as illustrated in Fig. 12. The cooling ducts have rectangular cross sections with a width w_{duct} of 30 mm, and a height h_{duct} of 5 mm, and are separated by 10 mm. The radial distances from the inner and outer frame boundaries $l_{Fr,lower}$ to the ducts are 3 mm on each side.

4.1.1. Frame conductive thermal resistance

For simplicity, only one network node is used for the whole frame. Another simplification is to only consider the radial heat transfer between the stator back surface and the lower/inner cooling duct walls. Therefore, the frame node is placed at half the radial distance between these two boundaries. This part can be considered to be a hollow cylinder with the inner and outer radii $r_{Fr,in}$ and $r_{Fr,in} + l_{Fr,lower}$, and the length of the active core l_{stk} , of

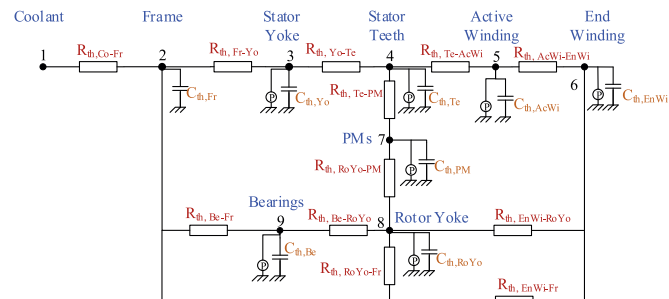


Fig. 11. Implemented thermal network.

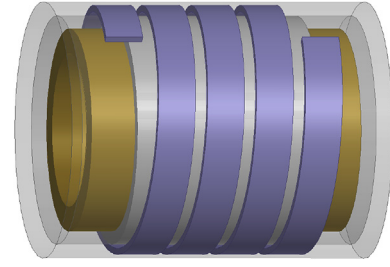


Fig. 12. The four laps spiral cooling channels with rectangular ducts, along with simplified frame, stator core and end windings.

150 mm. The conductive thermal resistance can then be expressed as

$$R_{th,Fr} = \frac{\ln\left(\frac{r_{Fr,in} + l_{Fr,lower}}{r_{Fr,in}}\right)}{2\pi\lambda_{Al}l_{stk}} \quad (1)$$

4.1.2. Cooling convection thermal resistance

In order to estimate the thermal convection resistance between the cooling media and the frame, the heat transfer coefficient is approximated. Preferably measurements or CFD methods are to be used for this purpose. Here, however, a rough empirical approach to find suitable Reynolds and Nusselt numbers is considered accurate enough.

The Prandtl number, Pr , of the coolant is much larger than one in the whole temperature range, as is shown in Fig. 13, hence convection dominate rather than conduction.

For circular tubes the flow can be assumed to be laminar when $Re \leq 2300$, and fully turbulent when $Re \geq 10^4$ [19,32,33]. According to Ref. [19], these critical values can also be applied to non-circular tubes. In practice, the critical Re values also depend on factors such as surface roughness and vibrations [32], which makes them difficult to predict.

The hydraulic diameter D_h is four times the cross sectional area divided by the perimeter [32,34]. For a rectangular tube, with side a and b , D_h is

$$D_h = \frac{2ab}{a+b} \quad (2)$$

The Reynolds number Re_D depends on D_h , the mass density ρ , the dynamic viscosity μ , and the average flow velocity v_{ave} (m/s) [19], which can be expressed as the volume flow rate $\dot{V}_{L/min}$ (liters/min), as

$$Re_D = \frac{\rho D_h v_{ave}}{\mu} = \frac{2\rho}{\mu(a+b)} \frac{\dot{V}_{L/min}}{60 \cdot 10^3} \quad (3)$$

Re_D as a function of flow rate is presented in Fig. 14a, for four

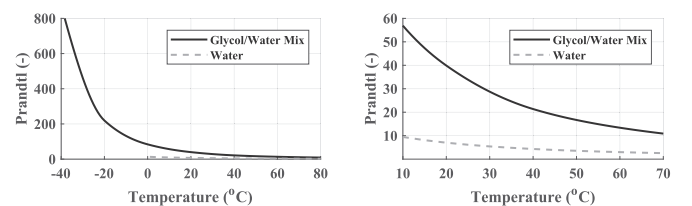


Fig. 13. The Prandtl number, Pr of the coolant as a function of temperature.

different coolant temperatures. The flow rate needed to reach the Re value for critically turbulent flow is lower when the coolant is warmer, and higher when the coolant is colder.

For fully developed **laminar** flow the Nusselt number, Nu , can be approximated as a constant that only depends on the cross sectional geometry [19,32–34]. For rectangular tubes with width-to-height ratio of 6 ($30/5 = 6$), and under the assumption of a constant heat flux, Nu is **6.05** [32]. For simplicity, the entrance effect is here neglected, even though it could locally result in up to three times larger Nu values.

For **turbulent** flow with Re_D in the range $3 \cdot 10^3 - 5 \cdot 10^6$ and Prandtl (Pr) 0.5–2000, Nu can be approximated to a reasonable accuracy [19,32,33,35], as

$$Nu = \frac{(f/8)(Re_D - 1000)Pr}{1 + 12.7(f/8)^{1/2}(Pr^{2/3} - 1)} \quad (4)$$

where the (Moody/Darcy) friction factor f , for smooth tubes can be approximated as

$$f = (0.790 \ln(Re_D) - 1.64)^{-2} \quad (5)$$

The surface roughness for die cast aluminum is here estimated to approximately $5 \mu\text{m}$. This gives a relative roughness (i.e. ratio of surface roughness to hydraulic diameter) of $6 \cdot 10^{-6}$. According to a Moody diagram in e.g. Ref. [19], the friction factor for this level of relative roughness may be approximated as that of a smooth surface for Re_D values lower than 10^5 , i.e. well within the expected Re_D range. Therefore, (5) is here used.

The resulting Nu number as a function of flow rate is shown in Fig. 14b, for different coolant temperatures. Similarly to the Re_D , the Nu number increases with both temperature and flow rate for turbulent flows.

The average heat transfer coefficient $h_{cool} = \lambda Nu / D_h$ ($\text{W/m}^2\text{K}$), is presented in Fig. 15 as a function of volume flow rate, for four different coolant temperatures. For laminar flow h_{cool} is almost constant for all flow rates and temperatures: around $290 \text{ W/m}^2\text{K}$. In contrast, for turbulent flow, h_{cool} increases with both flow rate and temperature and reach a few thousand $\text{W/m}^2\text{K}$ in the studied range. It is assumed that a turbulent flow is preferred. Therefore, in the case of 65°C coolant, a flow rate of 6 L/min is chosen, which gives an h_{cool} of $1988 \text{ W/m}^2\text{K}$. The temperature change (heat pick-up) of the coolant medium along the cooling channel is ignored, even though it may be up to 17°C .

Based on 2D thermal steady state simulations in Comsol Multiphysics, as in Fig. 16, it is assumed that 50% of the total heat flux between the stator back and the cooling channel will pass through the lower duct walls. Therefore, a correction factor $k_{conv, corr}$ of 0.5 is added to the convection thermal resistance of the cooling channel $R_{th, cool}$, which is.

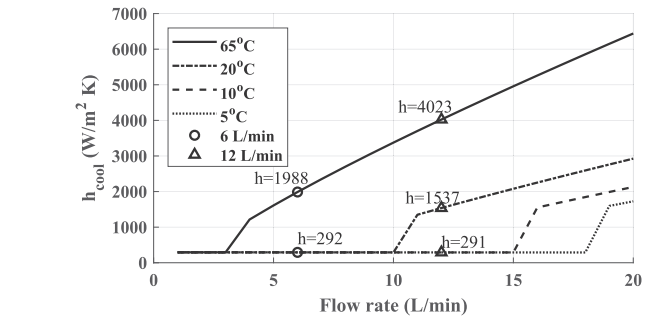
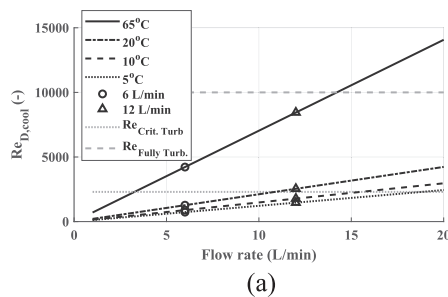


Fig. 15. The estimated average heat transfer coefficient of the coolant, as a function of flow rate and temperature.

$$R_{th, cool} = \frac{k_{conv, corr}}{h_{cool} A_{cool}} \quad (6)$$

where A_{cool} is the surface area of the inner cooling duct boundaries, as in

$$A_{cool} = 4 \cdot 2\pi w_{duct} (r_{Fr, in} + l_{Fr, lower}) \quad (7)$$

4.1.3. Thermal resistance between coolant and frame

The thermal resistance between the frame temperature node and the cooling channel's average temperature is thus the sum of the cooling convection thermal resistance and half of the conductive thermal resistance of the frame, as in

$$R_{th, Co-Fr} = R_{th, cool} + R_{th, Fr} / 2 \quad (8)$$

4.2. Stator yoke

As in [21, p.85], the thermal resistance of the stator yoke $R_{th, StYo}$, is modeled as a hollow cylinder consisting of stacked laminated sheets of electrical steel with perfect insulation, thereby assuming a strictly radial heat flow. The length of the cylinder is shorter than the core length due to the stacking factor.

4.2.1. Contact resistance between frame and stator yoke

Small air pockets inevitably exist between the aluminum frame and the stator back, who's size partly depend on the manufacturing process and surface roughness [1,36]. Due to the relatively low thermal conductivity of air they need to be considered. The air pockets can be modeled as a small equivalent air gap [36]. It is here assumed that the gap distance, $l_{contFr-Yo}$ is $10 \mu\text{m}$, i.e. the lower limit

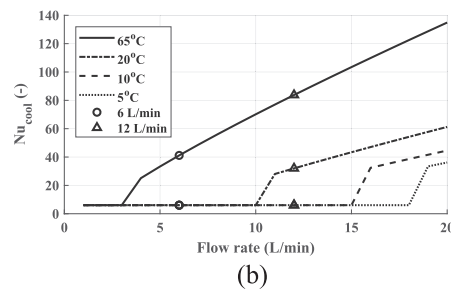


Fig. 14. Re and Nu of the coolant as a function of flow rate and temperature. (a) Re . (b) Nu .

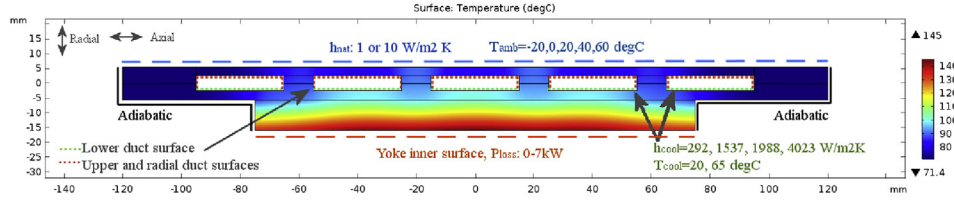


Fig. 16. Temperature distribution in 2D steady state simulation geometry in Comsol, for the case 65 °C coolant at 6 L/min, 7 kW of losses from stator yoke inner surface boundary, and zero ambient temperature with no natural convection to ambient.

in the reported measured range 0.01–0.077 mm in Ref. [36].

The contact resistance is modeled as a hollow cylinder, as

$$R_{th,ContFr-Yo} = \frac{\ln\left(\frac{r_{Yo,out} + l_{contFr-Yo}}{r_{Yo,out}}\right)}{2\pi\lambda_{Air}l_{stk}} \quad (9)$$

4.2.2. Thermal resistance between frame and stator yoke

The thermal resistance between the frame and the yoke nodes consist of half of the frame and yoke conductive resistances, as well as the contact gap resistance, as in

$$R_{th,Fr-Yo} = R_{th,Fr}/2 + R_{th,ContFr-Yo} + R_{th,StYo}/2 \quad (10)$$

4.3. Stator teeth

Only the radial heat flow is considered in the stator teeth, which is modeled as parallel thermal resistances. The same method as in [23, p.69–70] and in [21, p.87–88] is here used for the total radial thermal resistance of the teeth $R_{th,Te}$. Then the variation of the tooth width along the radial direction is expressed analytically.

4.3.1. Thermal resistance between stator yoke and teeth

The thermal resistance between the yoke and teeth node is half of the thermal resistance for each part, as

$$R_{th,Yo-Te} = R_{th,StYo}/2 + R_{th,Te}/2 \quad (11)$$

4.4. Stator winding

As copper losses are one of the main loss components in the motors the heat flow from the winding is large. This heat will pass through, not only the copper wires, but also the wire insulation, the impregnation, air pockets and the slot liner. Since the distributed stranded winding is not geometrically well determined a specific geometrical representation is not possible.

4.4.1. Thermal resistance between active winding and teeth

Again, the same method as in [23, p.59–63] and [21, p.88–93] is here used, where the slot is converted to an equivalent rectangular shape in order to determine the average slot temperature. The equivalent slot is then divided into two thin surface layers representing the slot liner of 0.2 mm and a thin air film of 10 μm, and where the rest of the volume consist of an equivalent winding mix representing copper and impregnation which is assumed to have a uniform heat generation.

The slot liner's and the winding impregnation's thermal conductivities are set to 0.2 W/mK, and the winding mix is set to 0.55 W/mK. The latter is approximated as 2.75 times that of the

impregnation material, as suggested in [23, p.60] for a 45% slot fill factor.

4.4.2. Thermal resistance between the active winding and end winding nodes

The thermal resistance between the active winding and end winding, $R_{th,AcWi-EnWi}$ is found as in [21, p.91–93], considering axial heat flow that occurs in all slots in parallel.

4.5. Air gap

Various suggested models of the air gap heat transfer can be found in publications, e.g. Refs. [1,21,23,27,36–39]. Many are based on the early work by Taylor 1935 [40], Gazley 1958 [41] and Becker and Kaye 1962 [42]. Usually the axial heat flow is omitted for machines with no internal forced air gap convection. The radial heat transfer is then dependent on the rotor speed, such that it is laminar i.e. conductive at low speed levels and transitional and turbulent at higher speed levels. The speed dependence is expressed by the Taylor number for which different critical values are set that represent laminar or turbulent flows. Different calculation methods are then given for the Nusselt number depending on the flow type.

The difference between the found models are usually the critical levels for the Taylor number which dictate the type of flow, and the approximation of the Nusselt number.

Here the method described in Ref. [42] is used, which is also used in Refs. [21,23,37–39], however with varying critical Taylor values.

The thermal resistance across the air gap is

$$R_{th,AG} = \frac{1}{h_{ag} A_{ag}} \quad (12)$$

where h_{ag} (W/m²K) is the air gap convection heat transfer coefficient, and A_{ag} (m²) the cylinder surface area in the air gap ($A_{ag} = 2\pi r_{ag} l_{stk}$), and r_{ag} (m) is the average air gap radius.

The heat transfer coefficient and the Nusselt number are related as in

$$h_{ag} = \frac{Nu \lambda_{air}}{2 l_{ag}} \quad (13)$$

where l_{ag} is the air gap length.

The Nusselt number is approximated for different ranges of the modified Taylors number as.

In [42] the critical value of the modified Taylors number

$Nu = 2$	$T_{am} < 1790$	laminar
$Nu = 0.128 \cdot T_{am}^{0.367}$	$1790 < T_{am} < 10^4$	transitional
$Nu = 0.409 \cdot T_{am}^{0.241}$	$10^4 < T_{am} < 10^7$	fully turbulent

between laminar and transitional flow is 1700, however, here the value is adjusted somewhat to avoid discontinuity at this transition.

Taylor's number T_a is

$$T_a = \frac{\rho_{air}^2 \omega_{rotor}^2 r_{ag} l_{ag}^3}{\mu_{air}^2} \quad (14)$$

where ρ_{air} (kg/m³) and μ_{air} (kg/ms) is the mass density and dynamic viscosity of air, respectively, and ω_{rotor} (rad/s) is the angular speed of the rotor.

The Modified Taylors number $T_{am} = \frac{T_a}{F_g}$ [39], is

$$T_{am} = Ta \frac{1697 \left[0.0056 + 0.0571 \left(\frac{2r_{ag} - 2.304l_{ag}}{2r_{ag} - l_{ag}} \right)^2 \right] \left[1 - \frac{l_{ag}}{2r_{ag}} \right]}{\pi^4 \left(\frac{2r_{ag} - 2.304l_{ag}}{2r_{ag} - l_{ag}} \right)} \quad (15)$$

where the geometrical correction factor F_g^{-1} is close to unity, and therefore often neglected.

The temperature dependence of the material parameters of air are considered, as shown in Fig. 28 in Appendix B. The air gap heat convection coefficient, and resulting thermal resistance at 20 °C and 100 °C are presented in Fig. 17, as a function of rotor speed. Since the air temperature is not calculated by the thermal network, the values at 100 °C are used in all cases.

4.6. Rotor, shaft and bearings

4.6.1. Magnets and rotor yoke

Since only radial heat flow is considered, the rather complex magnet v-shape is replaced by an equivalent geometry with arced magnets. This is only used in the calculation of the thermal resistance, as shown in Fig. 18 for one 8th of the rotor. Similar conversions methods are also seen in Refs. [24,26,43]. Additionally, a small air gap under the magnet is included with an assumed thickness of 150 μ m l_{MagGap} . The equivalent thermal resistance is then a mix of series and parallel connections in the rotor.

The equivalent rotor is divided into seven different segments: one lamination segment that is above the arced magnet (S4), and one that is below (S1); one that is the arced magnet (S7); one small air segment on each side of the magnet with same height as the magnet (S5, S6); and two lamination segments outside of the air segments (S2, S3).

Segment S1 and S4 are modeled as hollow cylinders, resulting in the expression

$$R_{th,RoS:1,4} = \frac{\ln\left(\frac{r_{out}}{r_{in}}\right)}{2\pi\lambda l_{stk}} \quad (16)$$

The heat flow in segment S2, S3, and S5–S7 as well as the small air gap under the magnet are modeled as pieces of a hollow cylinder as

$$R_{th,RoS:2,3,5-7} = \frac{\ln\left(\frac{r_{out}}{r_{in}}\right)}{\varphi n_{pole} \lambda l_{stk}} \quad (17)$$

where n_{pole} is the number of poles. Furthermore, the radial heat flow in segment S2,S3, and S5–S7 is assumed to occur in parallel, and their equivalent resistance is $R_{th,MagEq}$. The radii and angles used in the conversion is presented in Table 6, as noted in Fig. 18.

4.6.2. Thermal resistance between tooth and magnets

The magnet node is placed at half the thermal resistance of the magnet. The thermal resistance between the stator tooth network node and the magnet node is thus found as

$$R_{th,Te-PM} = R_{th,Te}/2 + R_{th,AG} + R_{th,RoS4} + R_{th,MagEq}/2 \quad (18)$$

4.6.3. Thermal resistance between magnets and rotor yoke

The rotor yoke node is placed at half the thermal resistance of the lower rotor part. The thermal resistance between the magnet network node and the rotor node then becomes

$$R_{th,RoYo-PM} = R_{th,MagEq}/2 + R_{th,MagAG} + R_{th,RoS1}/2 \quad (19)$$

4.6.4. Shaft

The shaft is assumed to be a lossless solid with only axial heat conduction, as also done in Refs. [21,27]. Furthermore, it is assumed to have a homogenous temperature distribution as in Ref. [21]. The shaft thermal resistance is divided into two sections depending on the shaft radius. Within the length of the lamination stack l_{stk} the shaft radius equals the rotor yoke inner radius $r_{RoYo,in}$. Outside of the lamination stack the shaft radius $r_{sh,ext}$ is 20 mm, and the distance to the bearings $l_{sh,ext}$ is 45 mm on each side.

Similarly as in Ref. [21], the shaft thermal resistance $R_{th,Sh}$ is then

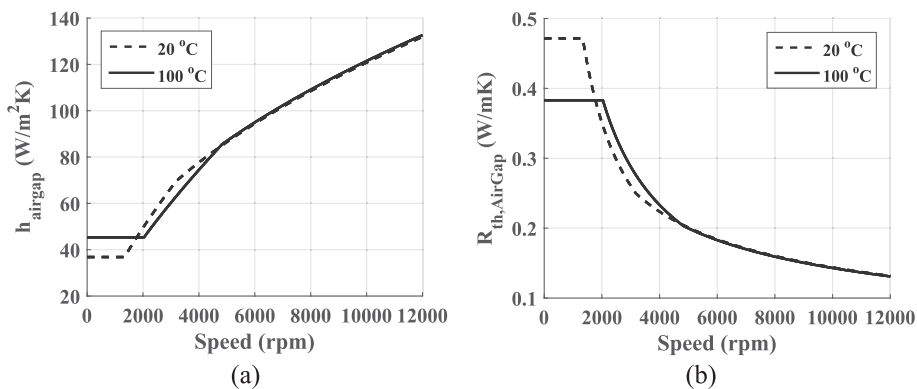


Fig. 17. Speed dependence of h_{airgap} and $R_{th,AirGap}$ in the air gap. (a) h_{airgap} . (b) $R_{th,AirGap}$.

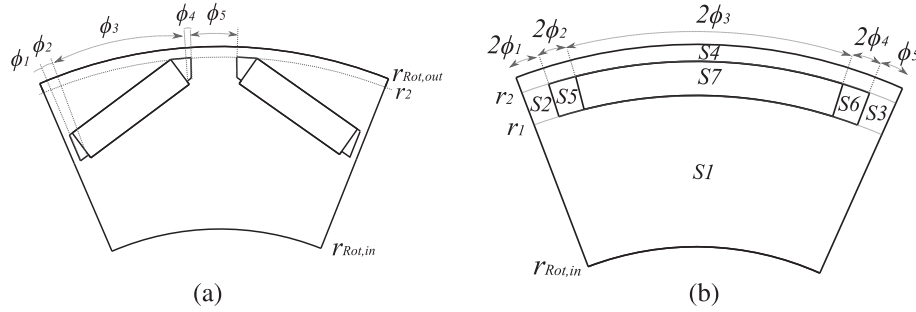


Fig. 18. Rotor geometries in electromagnetic and thermal equivalent models. (a) Electromagnetic rotor geometry. (b) Thermal equivalent rotor geometry outline.

Table 6

Parameters in the equivalent rotor geometry used in the thermal network.

Material	R_{th}	r_{out}	r_{in}	φ
Lamination	$R_{th,RoS1}$	r_1	$r_{Rot,in}$	2π
Lamination	$R_{th,RoS2}$	r_2	r_1	$2\varphi_1$
Lamination	$R_{th,RoS3}$	r_2	r_1	φ_5
Lamination	$R_{th,RoS4}$	$r_{Rot,out}$	r_2	2π
Air	$R_{th,RoS5}$	r_2	r_1	$2\varphi_2$
Air	$R_{th,RoS6}$	r_2	r_1	$2\varphi_4$
Magnet	$R_{th,RoS7}$	r_2	r_1	$2\varphi_3$
Air	$R_{th,MAGAG}$	$r_1 + l_{MagGap}$	r_1	$2\varphi_3$

$$R_{th,Sh} = \frac{l_{stk}}{\pi r_{RoYo,in}^2 \lambda_{steel}} + \frac{2l_{sh,ext}}{\pi r_{sh,ext}^2 \lambda_{steel}} \quad (20)$$

where λ_{steel} is the thermal conductivity of the shaft steel material.

4.6.5. Bearings

The thermal resistance of the bearings $R_{th,Be}$ is modeled as in Ref. [21], which is based on empirical data of IMs in Ref. [23], but where the speed dependent term is neglected for simplicity.

Also bearing losses are included in the thermal model, estimated [44] as

$$P_{loss,Be} = \frac{r_{Be} \mu_{Be} T_{rq,e} \omega_m}{r_{Rot,out}} \quad (21)$$

where $T_{rq,e}$ is the motor torque, ω_m is the motor angular speed, r_{Be} is the bearing bore radius (which equals the radius of the extended part of the shaft), μ_{Be} is the bearing friction coefficient which is here assumed to be 0.0015 as typical for deep groove ball bearings in Ref. [44].

4.6.6. Contact resistance between rotor yoke and shaft

A 10 μm air film $l_{contRoYo-Sh}$ is assumed between the rotor yoke and the shaft contact surfaces. Also the thermal resistance $R_{th,ContRoYo-Sh}$ of this contact gap is modeled as a hollow air cylinder.

4.6.7. Thermal resistance between bearings and frame

As suggested in Refs. [21,23], the thermal resistance between the bearing and the frame is

$$R_{th,Be-Fr} = R_{th,Be} / 4 \quad (22)$$

4.6.8. Thermal resistance between rotor yoke and bearings

The thermal resistance between rotor yoke and the bearings is

$$R_{th,Be-RoYo} = \frac{R_{th,YokeLow}}{2} + R_{th,ContRoYo-Sh} + \frac{R_{th,Sh}}{2} + \frac{R_{th,Be}}{4} \quad (23)$$

4.7. Internal air

The internal air is the air inside the frame except the air gap between the stator and rotor. Analytical modelling expressions are not applicable, rather empirical data must be used due to the complicated air flow paths in the geometrically complex region. Therefore, there are many published suggestions for modelling of the convective heat transfer in this region [1,23,45]. A comparison between different heat transfer coefficient expressions that are suggested in various publications, along with experimental results of end winding convection, are presented in Ref. [45] (and partly in Fig. 19). A fairly similar linear dependence on rotor speed is typically noted for the suggested heat transfer coefficients, with an offset which represents natural convection.

As suggested for the simple network in Ref. [23] and also used in Ref. [21], three separate convective heat transfer coefficients to the internal air are here implemented: one to the inner frame surface, one to the rotor end shields and one to the end windings.

The inner frame surface area consist of the two inner end cap surfaces and the inner frame shell surface that extends outside both sides of the lamination stack.

The rotor end shield area is approximated by the circular surface area with the average air gap radius.

As in Ref. [23], the surface area of the end winding is approximated as

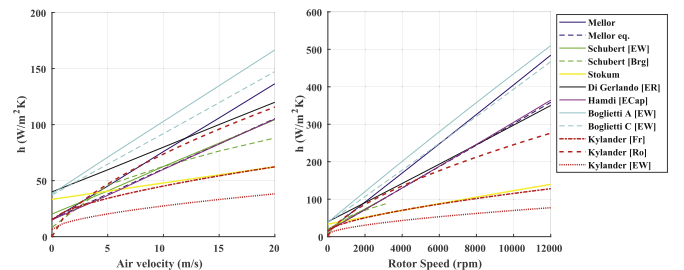


Fig. 19. Comparison of suggested internal air convection heat transfer coefficients. To the left: original data from references, to the right: extrapolated data for the used machine speed range. Mellor eq. from Ref. [1], Kylander from Ref. [23], the rest from Ref. [45].

$$A_{EnWi} = \pi l_{passive} r_{EnWi,ave} \quad (24)$$

where $l_{passive}$ is the average end winding conductor length, $r_{EnWi,ave}$ is the average radial distance for the end winding.

A comparison between different found suggested values of convection heat transfer coefficient is shown in Fig. 19. The speed range of found data are all up to 20 m/s, which represent about 3144 rpm of the here used motor. The rotor speed dependence in the right part of Fig. 19 is based on extrapolation of the velocity profiles. The Kylander [EW] data has the lowest speed dependence in this comparison, whereas the Boglietti data seem to have the largest. The Kylander [Fr] data are very similar to the Stokum data for higher speed levels. Between Kylander's three data sets, the [Ro] data has the largest speed dependence, which is reasonable since the air speed is probably higher closer to the rotor surface.

Since the internal air temperature is not a desired network node, the three thermal resistances to the internal air are converted from a Y to a Δ , as suggested in Ref. [23], forming $R_{th,RoYo-Fr}$, $R_{th,EnWi-RoYo}$ and $R_{th,EnWi-Fr}$.

4.8. Thermal capacitances

The thermal capacitance of each motor part is the product of the specific heat of the material and its mass, or density and volume.

For the thermal capacitance of the frame, the volume includes the two end caps and the whole frame cylinder, while excluding the volume of the cooling channel. To keep a 10 mm distance from the end winding to the inner side of the end cap, as the end winding extent varies between the different slot geometries, the cylindrical part of the frame also varies. Therefore, the frame mass is somewhat lower for the Small slot geometry, and higher for the Large and High slot geometries.

The thermal capacitance of the yoke is modeled as a hollow cylinder. The thermal capacitance of the stator teeth, magnets and the rotor laminations are found via the geometrical surface area from the FEA software, and the stack length.

The thermal capacitance of the active part of the winding is found by taking the sum of the active winding mass and the slot impregnation mass. The two volumes are found via the axial copper and slot cross sectional areas, the number of slots and the stack length.

The thermal capacitance of the end winding is found in a similar way as the active part of the winding, but the winding length is instead the passive part of half a turn, $l_{passive}$.

The shaft thermal capacitance is here neglected. This is considered a valid simplification as its thermal time constant is about 1 h and thus have little effect on the rotor and magnet temperatures, and even smaller on the stator laminations and windings.

The thermal capacitance of the bearings is found by using the motor part mass, and assuming that the specific heat is the same as for the shaft material.

The resulting network thermal capacitances are presented in Table C.11 in Appendix C. The values adhere to material parameters at 100 °C. As shown, the thermal capacitance of the end winding is generally lower than it is for the active winding.

4.9. Summary of thermal network node resistances

The resulting network thermal resistances are presented in Table C.10 in Appendix C. The thermal resistance values are considered to be well in line with the values in Ref. [21].

5. Calculation set-up of lumped-parameter thermal model

The thermal network calculation algorithm is presented in Fig. 20, with two types of inputs, first; a specific coolant temperature and flow rate, second; motor torque and speed operating points. Then the electromagnetic losses in the six motor parts for the three different magnet and copper temperatures are extracted for the specific operating points, along with bearing losses.

In the steady state solution for each operating point, an initial guess of the temperature in the magnet and winding network nodes is first used when updating the motor losses for the current temperatures, which is done via linear interpolation. Then follows an iterative loop in which both the temperatures and the losses are updated with respect to each other, until the temperature difference between the last two iterations fall below a specified threshold value.

In the transient solution, an initial temperature guess for the first value of the losses is done similarly as in the steady state case. However, then the temperature increase during one time step is calculated. In the next time step the losses are temperature corrected by using the temperatures from the previous time step.

In both the steady state and the transient solution, some temperature depending parameters are also updated. These are the copper and laminations' thermal conductivity and specific heat, and the thermal conductivity of steel, which is used in the shaft and bearings. The temperature dependencies of these parameters are presented in Appendix B.

5.1. Steady state validation with thermal FEA

As a frame of reference, a steady state comparison is conducted between the LPN and thermal simulation results from a 2D implementation of the motor in the FEA software Ansys Mechanical. Two motor operating points are considered: 100 Nm at 4000 rpm, and 50 Nm at 12000 rpm. The former represent a medium load situation where the total loss is 1.7 kW, and the latter a high load situation where the total loss is 3.6 kW. In both cases, the coolant temperature was set to 65 °C and the flow rate to 6 L/min.

In Ansys Mechanical the losses are implemented as averaged over the same motor regions as was used in the electromagnetic simulations. In order to make the two calculation procedures comparable the following set-up was used in the Ansys Mechanical 2D calculation. Both the active and the end winding parts of the copper losses are applied in the windings, since it is not possible to represent the end windings in the 2D structure. The heat flow through the shaft and internal air were calculated with the LPN, and then moved from the sending to the receiving regions manually. Moreover, the air gap is modeled as a conductive solid that has an equivalent thermal conductivity. This equivalent value is found from the LPN air gap thermal resistance, the air gap thickness and a surface area in the middle of the air gap.

The results are presented in Table 7, along with illustrations of the temperature distribution in one case from Ansys Mechanical in Fig. 21. For the medium load case the LPN temperatures are at most

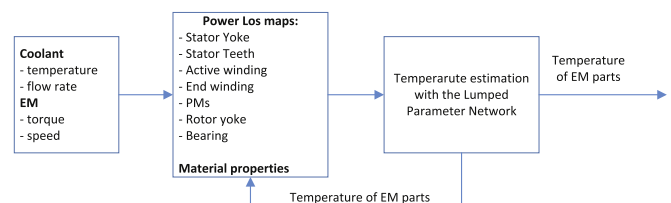


Fig. 20. Calculation loop for thermal performance of EM.

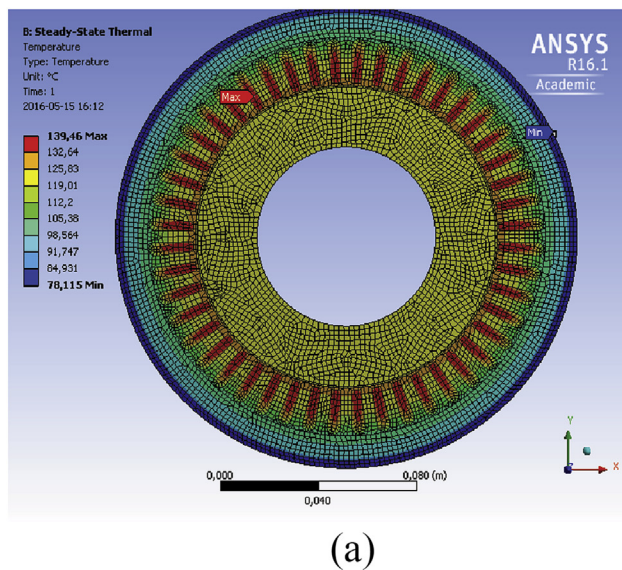
Table 7
Steady state temperature comparison in °C between the LPN and FEA software.

Motor Part	4000 rpm, 100 Nm			12000 rpm, 50 Nm		
	LPN	FEA	(Diff.)	LPN	FEA	(Diff.)
Frame	71.3	71.3	(0)	78.1	78.5	(-0.4)
Stator yoke	80.4	80.2	(0.2)	95.5	96.8	(-1.3)
Stator teeth	95.6	91.9	(3.7)	126.4	122.6	(3.8)
Active winding	103.2	102	(1.2)	138.0	139	(-1)
End winding	127.2	—	(—)	164.2	—	(—)
Magnets	93.9	91.7	(2.2)	123.7	120	(3.7)
Rotor yoke	92.9	91.4	(1.5)	120.2	118.1	(2.1)

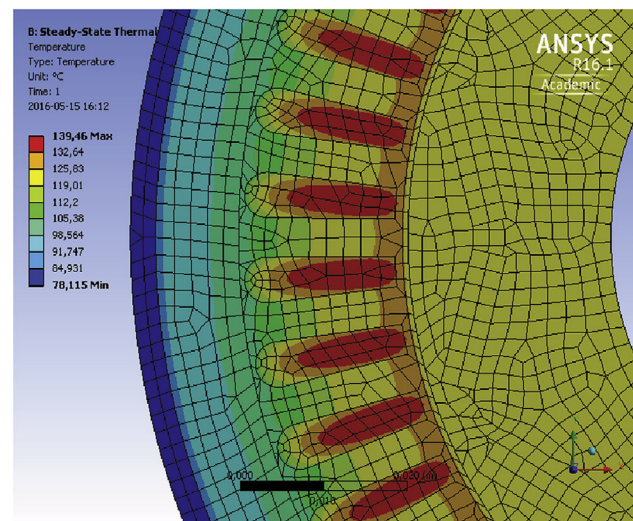
3.7 °C (4%) higher than the FEA solution. The largest deviation is seen for the stator teeth, the magnets, rotor yoke and the winding, which are over estimated by the LPN by 1.1%. At the high load, the LPN winding temperatures are up to 3.8 °C (3.1%) higher compared to the FEA solution. The largest deviations are seen in the same motor segments as for the medium load. The temperature agreement is deemed to be on an acceptable level.

6. Steady state performance

In order for the lifetime of the motor to be as long as possible it is

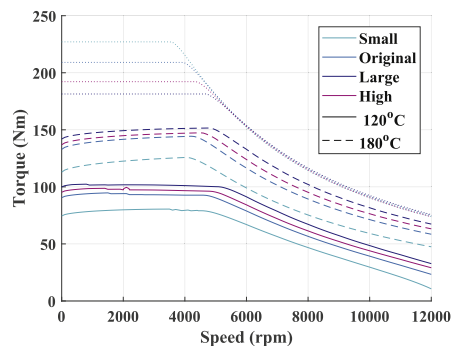


(a)

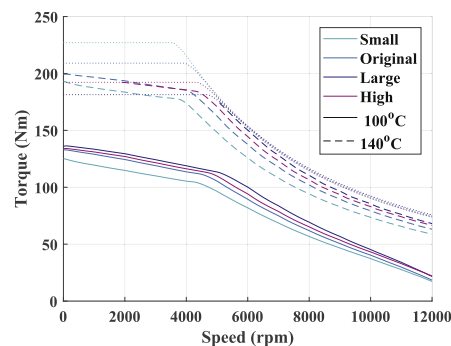


(b)

Fig. 21. Temperature distribution in the motor's axial cross section, at 12,000 rpm and 50 Nm load, with 65 °C coolant and 6 L/min. (a) Full cross section. (b) Zoom in.



(a)



(b)

Fig. 22. Steady state temperature development in end windings and magnets for all slot geometries, at a coolant temperature of 65 °C and a flow rate of 6 L/min. (a) End winding. (b) Magnets.

desired to limit the maximum temperature in the windings of an electric machine. The chosen critical temperature depends both on the winding insulation class and the number of working hours that is the design target [2].

The torque-speed levels for when the winding reach the temperatures 120 °C and 180 °C (insulation class H), and the magnet reach 100 °C and 140 °C, are presented for all four slot geometries in Fig. 22. As expected, it can be noted that the motor with the Small slot will reach both the winding and magnet temperatures at lower torque levels compared to the other slot geometries. The highest torque levels for the specified temperatures can be reached with the Large slot geometry. This is due to the lower losses, especially copper losses, in a large part of the motor operating area with the Large slot compared to the other geometries (presented in Fig. 9), and the higher losses for the Small slot.

7. Transient overload

Here the maximum time duration in a certain operating point in the torque-speed-plane is calculated, caused by a load step at a certain speed level. All load steps originates from the torque level where the end winding has already reached 120 °C in steady state. The initial steady state temperatures of all motor parts at this torque level are used as a starting point. Then load steps in the torque

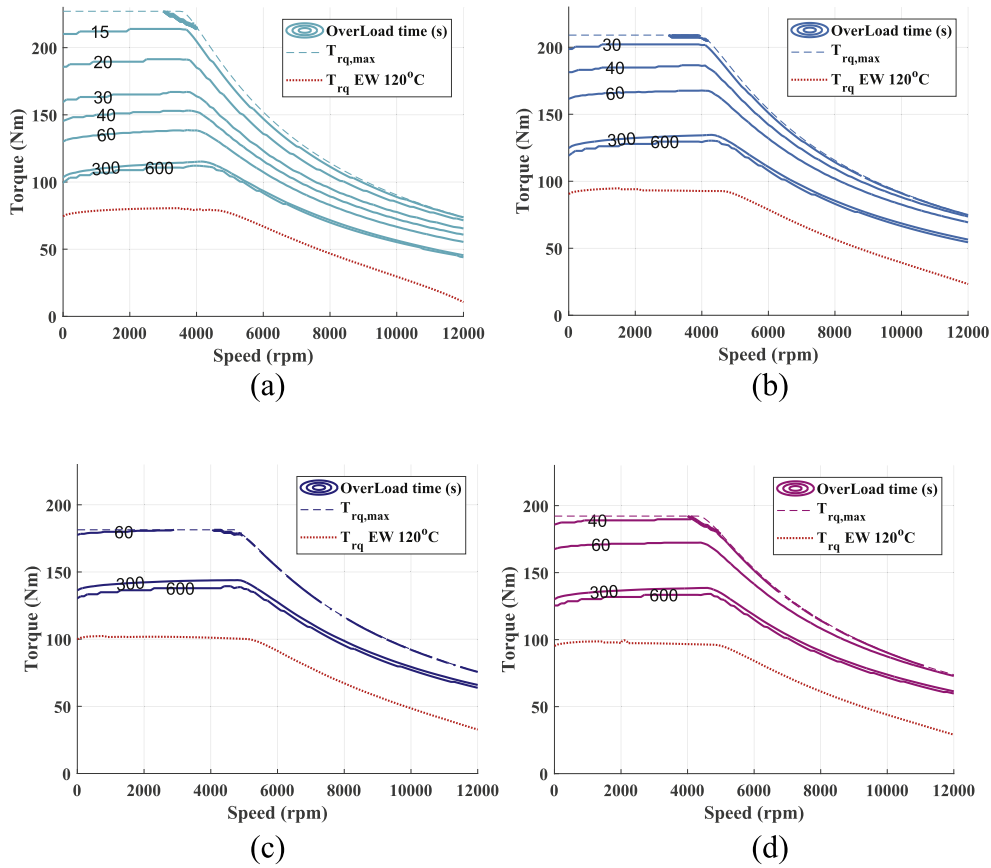


Fig. 23. Seconds spent in different operating points, before end winding reach 170 °C, at 65 °C coolant temperature, for the four slot sizes. (a) Small slot. (b) Original slot. (c) Large slot. (d) High slot.

level are taken, whereupon the time until the end winding reaches 170 °C is found via the transient thermal response, presented in Fig. 23.

As expected from the steady state results, the longest time at high torque levels can be sustained with the Large slot geometry. With a load step up to the peak torque level for the Large slot geometry it takes 60s until the end winding reaches the critical temperature of 170 °C. For the High slot to reach its peak torque level it takes 38s, for the Original 27s, and for the Small slot 13s. Considering that 80% of all accelerations in the used cycles are around 9s–13s [46], and that this is a worst case approach by using

a very high coolant temperature, the Small slot geometry may still be viable. It should also be noted that the comparison is done for a fixed max. phase current. In case of a higher inverter current rating, even larger torque levels could be thermally possible with the Original, Large and High slot geometries.

8. Drive cycle performance

On a flat road, the vehicle's instantaneous longitudinal wheel force F_{wheel} is the sum of the aerodynamic force, the rolling resistance, and the acceleration force as in

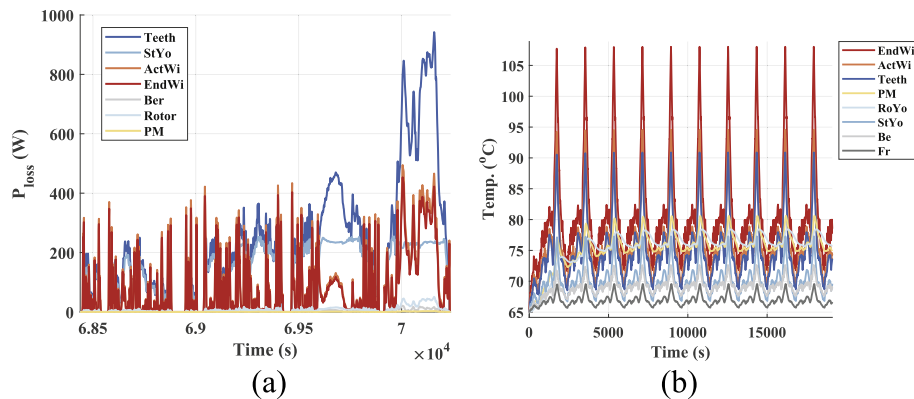


Fig. 24. Losses and temperature development during the WLTC cycle with the original slot, at a coolant temperature of 65 °C and a flow rate of 6 L/min. (a) Losses during one cycle. (b) Temperature during ten consecutive cycles.

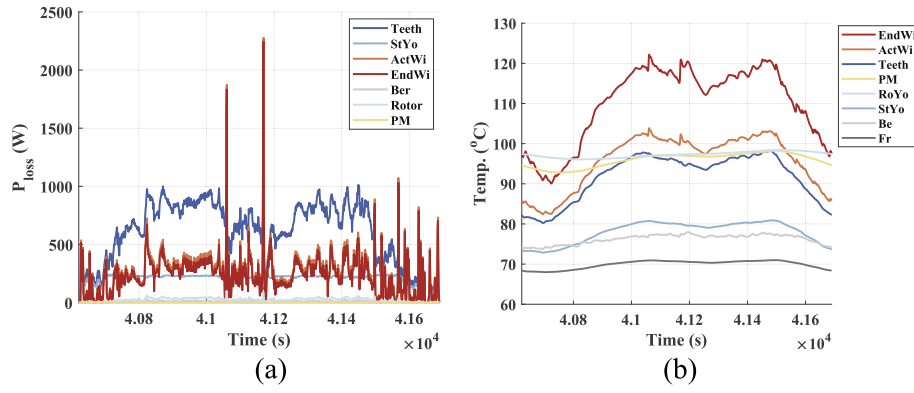


Fig. 25. Losses and temperature development during the ArtemisMW130 cycle with the original slot, at a coolant temperature of 65 $^{\circ}\text{C}$ and a flow rate of 6 L/min. (a) Losses. (b) Temperature.

$$F_{wheel} = \frac{1}{2} \rho C_d A v^2 + C_r m g + m \frac{dv}{dt} \quad (25)$$

where ρ is air density (1.2 kg/m³), v (m/s) longitudinal vehicle speed, m (kg) total rolling mass, g gravitational constant (9.81 m/s²). The used vehicle parameters are presented in Table D.12 in Appendix D. The wheel force relates to the electric machine torque T_{EM}

and speed n_{EM} via the wheel radius r , the transmission gear ratio k_{gear} and its efficiency η_{gear} (97%), in motoring mode as

$$T_{EM} = \frac{r F_{wheel,PT}}{\eta_{gear} k_{gear}} \quad (26)$$

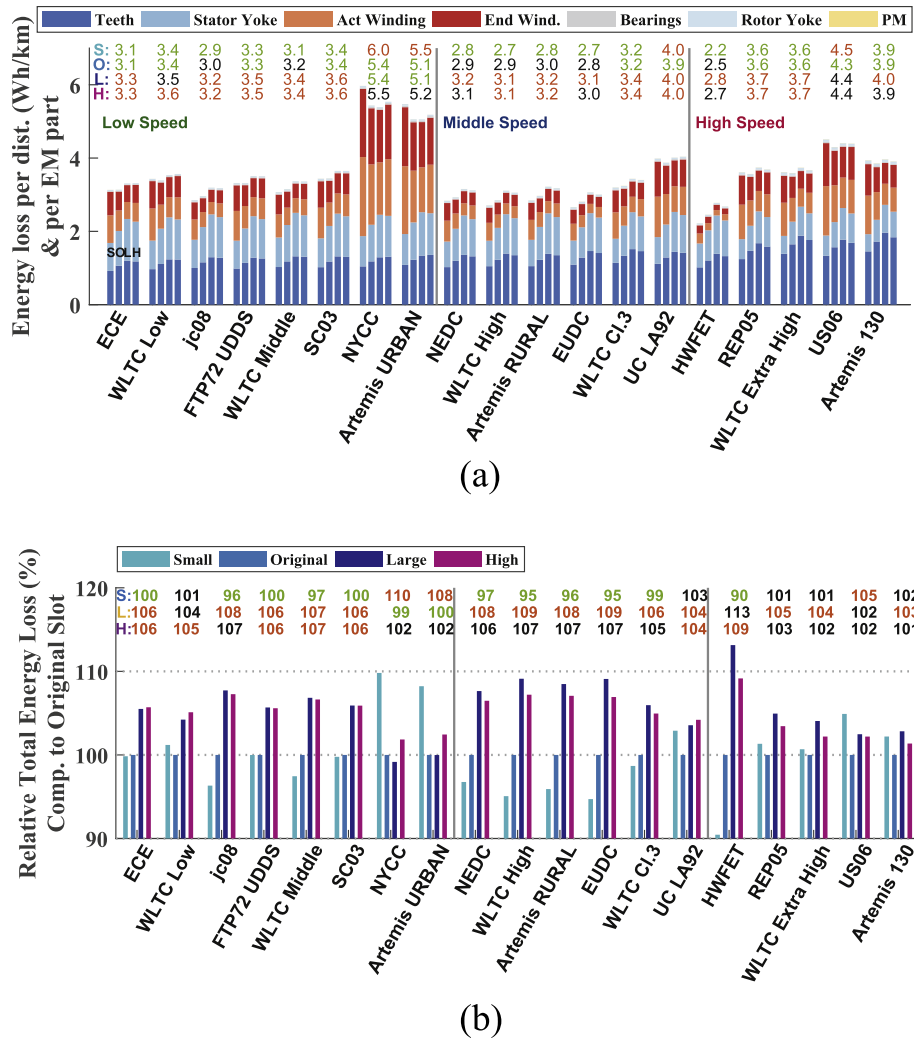


Fig. 26. Total energy losses during drive cycles divided by their total distance, including losses per motor part, as well as total energy losses normalized by the original slot's results, all at a coolant temperature of 65 $^{\circ}\text{C}$ and a flow rate of 6 L/min. (a) Total energy losses per distance. (b) Normalized cycle total energy losses.

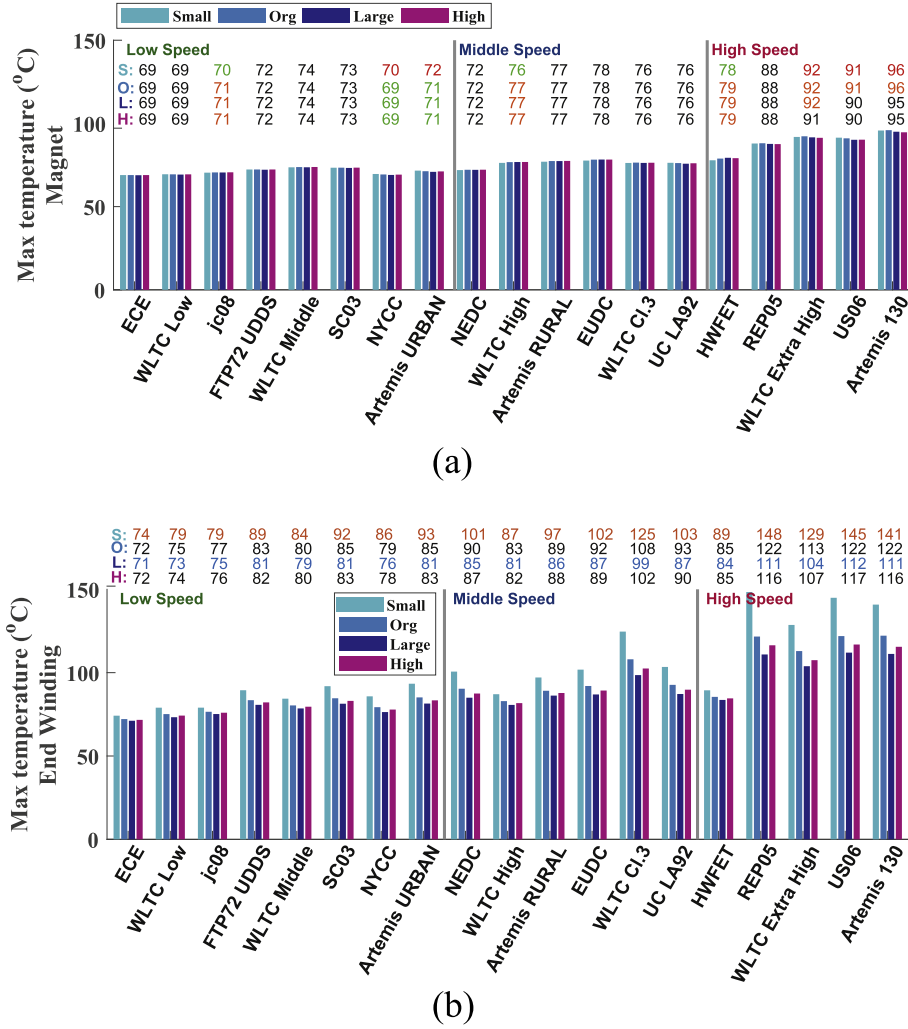


Fig. 27. Maximum magnet and end-winding temperatures during drive cycles, at a coolant temperature of 65 °C and a flow rate of 6 L/min. (a) Maximum magnet temperature. (b) Maximum end-winding temperature.

$$n_{EM} = k_{gear} \frac{v}{r} \frac{60}{2\pi} = k_{gear} w_{wheel} \frac{60}{2\pi} \quad (27)$$

where the wheel rotational speed w_{wheel} (rad/s) is the ratio of vehicle speed and wheel radius. The k_{gear} value is the ratio of maximum motor to wheel speed. The instantaneous wheel power, P_{wheel} , is the product of the wheel force and vehicle speed ($P_{wheel} = v F_{wheel}$). In each operating point of the drive cycles, the machine losses are extracted from generated loss maps based on previous description. The same loss maps are used in motoring and generative mode of operation.

With a coolant flow rate of 6 L/min at 65 °C, the motor's temperature development during selected Low, Middle and High speed drive cycles are investigated and compared between the different stator geometries. The cycles are further described in Ref. [15]. The cycles are repeated several times in order to reach thermal steady state. As an example, the motor part losses and temperature development during WLTC is presented in Fig. 24, and during ArtemisMW130 in Fig. 25. The teeth losses are the highest during high speed driving in both cycles. Large power loss peaks are reached during breaking in the ArtemisMW130 cycle, which cause a temperature rise in the end winding of around 9–12 °C during 4s

and 5s respectively. The end winding temperatures are the highest in all cycles.

The total energy losses for the studied drive cycles divided by their driven distance, including losses per motor part, are presented in Fig. 26a and the total energy losses normalized with the Original slot results are shown in Fig. 26b. For each cycle the order of the bars are from left to right; Small, Original, Large and High slot. In eleven of the cycles, the losses are the lowest with the Small slot, and in six with the Original slot. The Large slot gives the lowest losses for the two low speed cycles with a larger share of acceleration (NYCC, ArtemisURBAN). A larger acceleration content means more time spent on higher torque levels, which is why the winding losses are higher for such cycles. The difference between the winding and core losses is the largest for the low speed but aggressive cycles NYCC and ArtemisURBAN, hence the difference between the Small slot and the other geometries is also among the largest for these two cycles. As a sensitivity check, the drive cycle results were also calculated for the two cases of increasing and decreasing the gear ratio by 10%. Decreasing the gear ratio cause a shift of the drive cycle machine operating points towards lower machine speed. Then, in ten of the cycles, the total energy losses are the lowest with the Original slot, in seven with the Small and still in two with the Large slot. When increasing the gear ratio, the losses

are the lowest in twelve of the cycles with the Small slot, and in seven with the Original. Hence, a reduced gear ratio favors the Original slot over the Small, whereas the opposite applies for an increased gear ratio. This shift in order is only seen for low speed cycles.

The maximum reached magnet and end winding temperatures during the drive cycles are presented in Fig. 27. The maximum magnet temperature differ up to 1 °C between the different slot geometries for the investigated drive cycles. The highest magnet temperatures are seen for the two cycles with the highest average speed levels, but still they do not reach more than 96 °C.

The maximum end-winding temperature is the highest for the Small slot geometry for all cycles, followed by the Original slot, and the lowest for the Large slot geometry. As with the magnet, the largest peak temperatures are noted for the cycles with the highest speed levels, but still remain below 150 °C. A higher winding temperature may lead to a shorter lifetime of the winding insulation.

9. Conclusion

The aim of this paper is to conduct a focused electric machine design study, that is highly relevant in the development towards increased purpose designed electric drive trains. In this paper, the slot size (along with the copper area) for a PMSM reference motor is varied while the gross fill factor as well as current and voltage ratings are kept unchanged, hence the amount of losses are shifted between the winding and core. A machine with four differently sized slot areas named Small, Original, High, and Large, are evaluated electromagnetically with FEA and thermally with a lumped parameter network model.

The specific contributions of the paper are firstly, to compare the four machine's part and total losses in their torque-speed operating area as well as their peak torque envelope at a certain magnet temperature. Secondly, using a lumped parameter thermal network, to determine the four machines continuous and transient overload torque capability. Finally, and thirdly, to quantify the machine's energy losses and reached peak winding and magnet temperatures during 19 low, middle and high-speed official drive cycles.

As expected, a smaller slot increases the copper losses and decreases the iron losses (due to a widened magnetic path) as well as increases the produced peak torque for a given current rating. It would also result in a lower material cost since it has the least copper. The opposite then applies for a larger slot, which leads to higher thermally limited continuous and transient overload torque capability. The machine with the largest slot area is capable of staying at its peak torque for 60 s, whereas the respective duration is 27 s, 38 s, and 13 s for the Original, High and Small slot geometries.

In contrast, during 13 of the drive cycles, the energy losses with the largest slot were the highest due to its relatively higher part load (i.e. core) losses. Simultaneously, in 11 of the cycles the losses were the lowest with the smallest slot. However, since the winding losses are the highest with the Small slot, its peak winding temperature is the highest during all cycles.

Finally, despite being a case-study applied to a specific machine, it can be expected that the trends of the results do persist for similar machine types of not too different dimensions. Consequently, selection of a suitable electric machine design is strongly coupled to the specific application and its related boundary conditions. The analysis presented in this paper is therefore one plausible method to quantify comparable properties and evaluate designs for optimization.

CRedit authorship contribution statement

Emma Arfa Grunditz: Conceptualization, Methodology, Investigation, Formal analysis, Software, Validation, Visualization, Data curation, Writing - original draft, Writing - review & editing. **Torbjörn Thiringer:** Funding acquisition, Conceptualization, Methodology, Software, Validation. **Joachim Lindström:** Methodology, Investigation, Formal analysis, Software, Validation. **Sonja Tidblad Lundmark:** Funding acquisition, Conceptualization, Validation. **Mikael Alatalo:** Conceptualization, Validation.

Declaration of competing interest

The authors declare that they have no known competing financial interests or personal relationships that could have appeared to influence the work reported in this paper.

Acknowledgements

The financial support through Chalmers Area of Advance Transport (AoAT) is gratefully appreciated.

Appendix A. Machine Description

The frame is a hollow cylinder with an end cap on each side, all with a thickness of 11 mm, without complex textures. The outer frame diameter is 102 mm and the length 262 mm. The shaft has a length of 306 mm and a diameter of 40 mm except for the part along the lamination stack, which extend to the inner rotor lamination boundary (i.e. a diameter of 72.8 mm). The ball bearings have a width of 15 mm, and inner and outer diameters of 40 mm and 68 mm respectively. The mass of one unit is 190 g, as is commonly found for this size of ball bearings from the bearing manufacturer SKF [47].

The length of the end winding is estimated as the sum of the axial extent (on each side of the stack) and 1.2τ , where τ is the winding pole pitch [21, paper D p.92]. The axial extent is taken to be linearly proportional to the square root of the change in copper area from the original slot area to the others. For the small slot geometry, the extent on one side is shorter (29.7 mm), for the Large and High slot geometries it is longer (40.2 mm, and 37.2 mm respectively), than for the Original slot (35 mm).

Appendix B. Material Data

The density, thermal conductivity and specific heat of used materials are presented in Table B8.

Table B.8

Material properties of motor parts at 300K (assumed for magnets and impregnation).

	Mass Density (kg/m ³)	Thermal Conductivity (W/m K)	Specific Heat (J/kg K)
Air	1.1614	0.0263	1007
Frame	2790	168	883
Lamination	7540	21	464
Winding	8933	401	385
Impregnation	1350	0.2	1700
Magnets	7500	7.5	410
Shaft	7817	51.9	446

The copper and magnet material data at the temperatures 20 °C, 70 °C and 120 °C are shown in Table B9.

Table B.9

Magnet and copper material parameters at three temperatures.

	20 °C	70 °C	120 °C
B_r	1.236 T	1.1824 T	1.1244 T
100%		95.66%	90.96%
μ_r	1.0432	1.0428	1.0446
H_c	−942,926 A/m	−902,285 A/m	−856,586 A/m
σ	769,231 S/m	750,469 S/m	732,601 S/m
σ_{Cu}	59,523,809 S/m	49,890,042 S/m	42,940,275 S/m

The core losses per unit mass or volume are calculated in the FEM software as

$$P_{fe} = k_h f B_{pk}^n + k_c f^2 B_{pk}^2 \quad (B.1)$$

where.

k_h hysteresis coefficient

k_c eddy current coefficient

f (Hz) frequency of the flux

B_{pk} (T) maximum amplitude of the flux density

n depends on B_{pk} , f , and steel material (typically 1.6–2.2)

Based on the loss data of NO30, the following core loss coefficients are used: $k_h = 443.117 \text{ Ws}/(\text{m}^3 \text{ T}^2)$, $k_c = 0.201628 \text{ Ws}^2/(\text{m}^3 \text{ T}^2)$, and $n = 2$, as approximated by Ansys Maxwell. The temperature dependence of material parameters of air is presented in Fig. B28, thermal conductivity and specific heat, for the used lamination core material is presented in Fig. B29, thermal conductivity and specific heat, for copper (the used winding material) is presented in Fig. B30, and thermal conductivity for the used shaft material (carbon-silicon steel) is presented in Fig. B31.

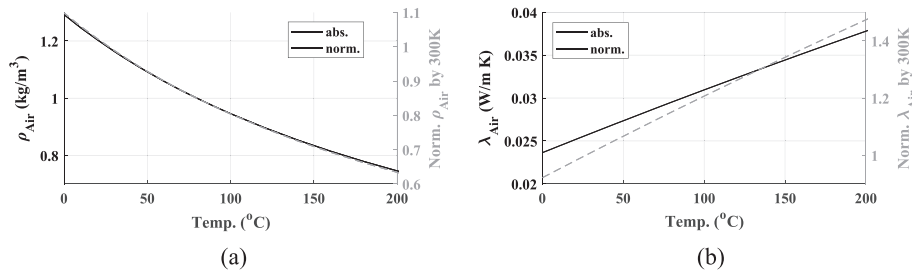


Fig. B.28. Air material properties as a function of temperature, both absolute values and normalized to the value at 20 °C [32]. (a) Density. (b) Thermal conductivity.

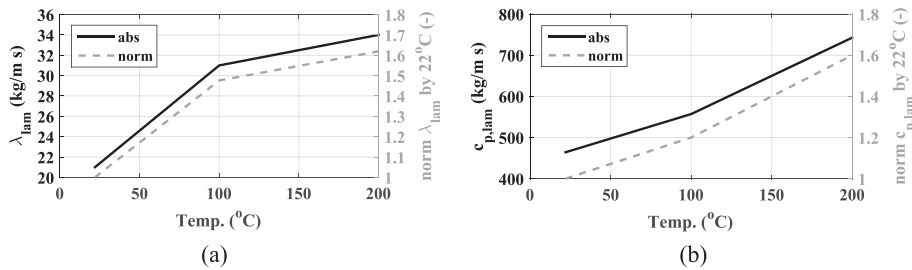


Fig. B.29. Thermal conductivity and specific heat of lamination material (NO30) as a function of temperature [48], both absolute values and normalized to the value at 22 °C. (a) Thermal conductivity. (b) Specific heat.

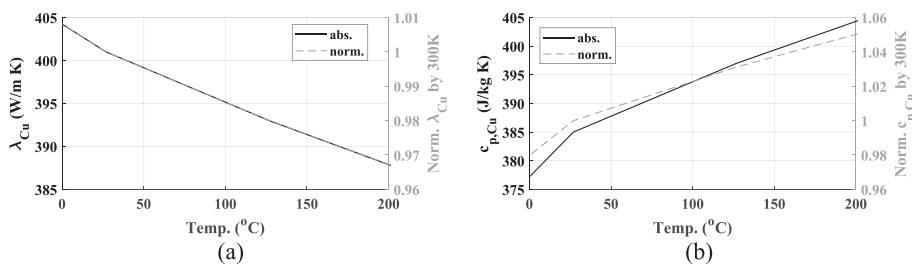


Fig. B.30. Thermal conductivity and specific heat of copper as a function of temperature [32], both absolute values and normalized to the value at 300 K. (a) Thermal conductivity. (b) Specific heat.

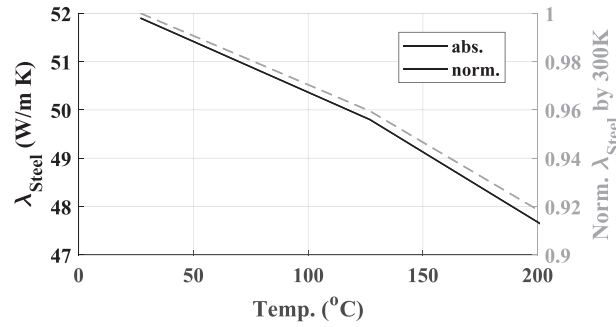


Fig. B.31. Shaft material thermal conductivity as a function of temperature, both absolute values and normalized to the value at 300 K [32].

Cooling medium (ethylene-glycol) material parameters as a function of temperature, is presented in Fig. B.32 (data from Ref. [31]). Fig. B.32 also include material parameters for water [32] as a reference.

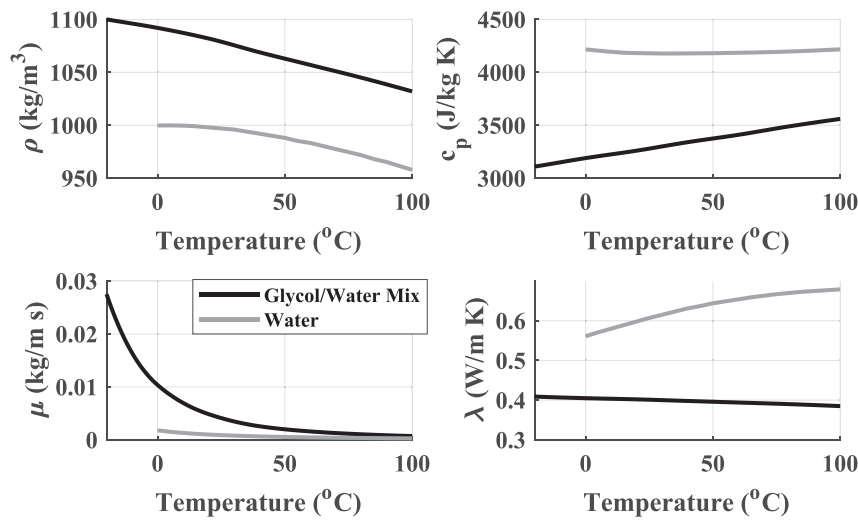


Fig. B.32. Glycol/water mixed coolant material properties as a function of temperature [31]. The properties of water are also included as a reference [32].

Appendix C. Thermal Impedance

The thermal resistances and capacitances are presented in Table C.10 and Table C.11. The values adhere to a coolant temperature of 65°C, a flow rate of 6 L/min and a rotor speed of 4000 rpm.

Table C.10

Thermal resistances (W/m K) in the thermal network for the four slot sizes.

	Small	Original	Large	High
$R_{th,Co-Fr}$	0.0037	0.0037	0.0037	0.0037
$R_{th,Fr-Yo}$	0.0066	0.0060	0.0055	0.0055
$R_{th,Yo-Te}$	0.0098	0.0115	0.0112	0.0115
$R_{th,Te-AcWi}$	0.0092	0.0084	0.0079	0.0076
$R_{th,AcWi-EnWi}$	0.0889	0.0669	0.0526	0.0603
$R_{th,EnWi-RoYo}$	1.3527	1.3002	1.2540	1.2665
$R_{th,Te-PM}$	0.2459	0.2482	0.2483	0.2483
$R_{th,RoYo-PM}$	0.1446	0.1446	0.1446	0.1446
$R_{th,EnWi-Fr}$	0.3422	0.3080	0.2796	0.3507
$R_{th,Be-RoYo}$	1.2464	1.3301	1.4123	1.3649
$R_{th,RoYo-Fr}$	0.5153	0.5150	0.5153	0.5169
$R_{th,Be-Fr}$	0.2450	0.2450	0.2450	0.2450

Table C.11

Thermal capacitances in J/K in the thermal network for the four slot sizes.

		Small	Original	Large	High
Frame	$C_{th,Fr}$	4403	4568	4729	4636
Stator yoke	$C_{th,Yo}$	4039	3345	2631	2631
Stator teeth	$C_{th,Te}$	2686	2725	2695	3136
ActWind.+insl.	$C_{th,AcWi}$	1247	1716	2251	1934
EndWind.	$C_{th,EnWi}$	576	871	1250	1026
Magnets	$C_{th,PM}$	501	501	501	501
Rotor yoke	$C_{th,RoYo}$	3717	3717	3717	3717
Bearings	$C_{th,Be}$	169	169	169	169

Appendix D. Vehicle Data

The parameters and requirements of the used vehicle is presented in Table D.12.

Table D.12

Data of the car used, also used in Ref. [17].

	Value	Unit
Curb weight, m	1700	kg
Front Area, A	2.3	m ²
Aerod. drag coeff. C_d	0.29	—
Wheel radius, r	0.32	m
Rolling resist. coeff. C_r	0.007	—
Gear ratio	9.984	—
Acceleration 0–100 km/h	10	s
Top speed	145	km/h

References

- [1] Mellor P, Roberts D, Turner D. Lumped parameter thermal model for electrical machines of tefc design, Electric Power Applications. IEE Proceedings B 1991;138(5):205–18. <https://doi.org/10.1049/ip-b.1991.0025>.
- [2] Huang Z, Márquez-Fernández FJ, Loayza Y, Reinap A, Alaküla M. Dynamic thermal modeling and application of electrical machine in hybrid drives. In: 2014 international conference on electrical machines (ICEM); 2014. p. 2158–64. <https://doi.org/10.1109/ICELMACH.2014.6960483>.
- [3] Boglietti A, Cavagnino A, Staton D. Determination of critical parameters in electrical machine thermal models, Industry Applications. IEEE Trans 2008;44(4):1150–9. <https://doi.org/10.1109/TIA.2008.926233>.
- [4] Fatemi A, Demerdash NAO, Ionel DM, Nehl TW. Large-scale electromagnetic design optimization of pm machines over a target operating cycle. In: 2015 IEEE energy conversion congress and exposition (ECCE); 2015. p. 4383–90. <https://doi.org/10.1109/ECCE.2015.7310279>.
- [5] Sizov GY, Ionel DM, Demerdash NAO. Multi-objective optimization of pm ac machines using computationally efficient - fea and differential evolution. In: 2011 IEEE international electric machines drives conference (IEMDC); 2011. p. 1528–33. <https://doi.org/10.1109/IEMDC.2011.5994836>.
- [6] Dominguez-Olavarria G, Márquez-Fernández FJ, Fyhr P, Reinap A, Andersson M, Alaküla M. Optimization of electric powertrains based on scalable cost and performance models. IEEE Trans Ind Appl 2019;55(1): 751–64. <https://doi.org/10.1109/TIA.2018.2864943>.
- [7] López-Torres C, García Espinosa A, Riba J, Romeral L. Design and optimization for vehicle driving cycle of rare-earth-free synrm based on coupled lumped thermal and magnetic networks. IEEE Trans Veh Technol 2018;67(1): 196–205. <https://doi.org/10.1109/TVT.2017.2739020>.
- [8] Martinovi M, Zarko D, Stipetic S, Jerić T, Kovacić M, Hanić Z, Staton D. Influence of winding design on thermal dynamics of permanent magnet traction motor. In: 2014 international symposium on power electronics, electrical drives, automation and motion; 2014. p. 397–402. <https://doi.org/10.1109/SPEEDAM.2014.6872026>.
- [9] Huang Y, Zhu Z, Guo B, Lin H, Fang S. Design and thermal analysis on high torque low speed fractional-slot concentrated windings in-wheel traction motor. In: 2016 XXII international conference on electrical machines (ICEM); 2016. p. 1487–92. <https://doi.org/10.1109/ICELMACH.2016.7732720>.
- [10] Jürgens J, Brune A, Ponick B. Electromagnetic design and analysis of a salient-pole synchronous machine with tooth-coil windings for use as a wheel hub motor in an electric vehicle. In: 2014 international conference on electrical machines (ICEM); 2014. p. 744–50. <https://doi.org/10.1109/ICELMACH.2014.6960264>.
- [11] Redlich J, Juergens J, Brune K, Ponick B. Synchronous machines with very high torque density for automotive traction applications. In: 2017 IEEE international electric machines and drives conference (IEMDC); 2017. p. 1–8. <https://doi.org/10.1109/IEMDC.2017.8002283>.
- [12] Wrobel R, Williamson SJ, Simpson N, Ayat S, Yon J, Mellor PH. Impact of slot shape on loss and thermal behaviour of open-slot modular stator windings. In: 2015 IEEE energy conversion congress and exposition (ECCE); 2015. p. 4433–40. <https://doi.org/10.1109/ECCE.2015.7310286>.
- [13] Emmrich K, Brune A, Ponick B. Evaluation of an analytical, efficiency-optimized torque-speed characteristic of induction machines coupled with a thermal-electromagnetic energy consumption calculation. In: 2014 international conference on electrical machines (ICEM); 2014. p. 762–7. <https://doi.org/10.1109/ICELMACH.2014.6960267>.
- [14] Goss J, Mellor PH, Wrobel R, Staton DA, Popescu M. The design of ac permanent magnet motors for electric vehicles: a computationally efficient model of the operational envelope. In: 6th IET international conference on power electronics, machines and drives (PEMD 2012); 2012. p. 1–6. <https://doi.org/10.1049/cp.2012.0251>.
- [15] Grunditz EA, Thiringer T. Performance analysis of current bevs based on a comprehensive review of specifications. IEEE Trans Transport Electrification 2016;2(3):270–89. <https://doi.org/10.1109/TTE.2016.2571783>.
- [16] Burress T, Campbell S. Benchmarking ev and hev power electronics and electric machines. In: Transportation electrification conference and expo (ITEC), 2013 IEEE; 2013. p. 1–6. <https://doi.org/10.1109/ITEC.2013.6574498>.
- [17] Arfa Grunditz E, Thiringer T. Electric vehicle acceleration performance and motor drive cycle energy efficiency trade-off. In: 2018 XIII international conference on electrical machines (ICEM); 2018. p. 717–23. <https://doi.org/10.1109/ICELMACH.2018.8507201>.
- [18] Grunditz EA, Lundmark ST, Alatalo M, Thiringer T. A. Nordel"of, Three traction motors with different magnet materials – influence on cost, losses, vehicle performance, energy use and environmental impact. In: 2018 thirteenth international conference on ecological vehicles and renewable energies (EVER); 2018. p. 1–13. <https://doi.org/10.1109/EVER.2018.8362387>.
- [19] Incropera F, Dewitt D, Bergman T, Lavine A. Fundamentals of heat and mass transfer. John Wiley & Sons; 2007.
- [20] Hi-lite no30 data sheet. 2015. accessed 2015-05-19, http://cogent-power.com/cms-data/downloads/Hi-Lite_NO30.pdf.
- [21] Lindström J. Development of an experimental permanent-magnet motor drive, Licentiate of engineering, Chalmers University of Technology; apr 1999. technical report no. 312L.
- [22] Neodymium-iron-boron magnets neomax. Hitachi Metals Ltd.; 2015. home page, accessed 2015-05-27, URL, http://www.hitachi-metals.co.jp/e/products/auto/el/p03_21.html.
- [23] Kylander G. Thermal modelling of small cage induction motors, Thesis for the degree of doctor of philosophy in engineering, Chalmers University of Technology; Feb 1995. technical report no. 265.
- [24] EL-Refaie A, Harris N, Jahns T, Rahman K. Thermal analysis of multibarrier interior pm synchronous machine using lumped parameter model, Energy Conversion. IEEE Trans 2004;19(2):303–9. <https://doi.org/10.1109/TEC.2004.827011>.
- [25] Juris P, Brune A, Ponick B. A coupled thermal-electromagnetic energy consumption calculation for an electric vehicle with wheel hub drive considering different driving cycles. In: Vehicle power and propulsion conference (VPPC), 2012 IEEE; 2012. p. 28–31. <https://doi.org/10.1109/VPPC.2012.6422655>.
- [26] Abdelli A. Optimal design of an interior permanent magnet synchronous motor for wide constant-power region operation: considering thermal and electromagnetic aspects. SAE Int. J. Alt. Power. 2014;3:129–38. <https://doi.org/10.4271/2014-01-1889>.
- [27] Boglietti A, Cavagnino A, Lazzari M, Pastorelli M. A simplified thermal model for variable-speed self-cooled industrial induction motor, Industry Applications. IEEE Trans 2003;39(4):945–52. <https://doi.org/10.1109/TIA.2003.814555>.
- [28] Dajaku G, Gerling D. An improved lumped parameter thermal model for electrical machines. In: 17th International conference on electrical machines (ICEM2006); 2006.
- [29] Fan J, Zhang C, Wang Z, Strangas E. Thermal analysis of water cooled surface mount permanent magnet electric motor for electric vehicle. In: Electrical machines and systems (ICEMS), 2010 international conference on; 2010. p. 1024–8.
- [30] Hendershot J, Miller T. Design of brushless permanent-magnet machines. Motor Design Books LLC; 2010.
- [31] accessed 2016-02-02 Table 8-3-1 - Properties of Mixture Water/Glycol. 1991. URL, https://detector-cooling.web.cern.ch/detector-cooling/data/Table_8-3-1.htm.
- [32] Çengel YA. Introduction to thermodynamics and heat transfer. Mcgraw-Hill; 2008.
- [33] Mills AF. Heat transfer. Prentice-Hall Inc.; 1999.
- [34] Holman JP. Heat transfer. ninth ed. Mcgraw-Hill; 2002.
- [35] Staton DA, Cavagnino A. Convection heat transfer and flow calculations suitable for electric machines thermal models. IEEE Trans Ind Electron 2008;55(10):3509–16. <https://doi.org/10.1109/TIE.2008.922604>.
- [36] Staton D, Boglietti A, Cavagnino A. Solving the more difficult aspects of electric motor thermal analysis in small and medium size industrial induction motors, Energy Conversion. IEEE Trans 2005;20(3):620–8. <https://doi.org/10.1109/TEC.2005.847979>.
- [37] Demetriades G, De La Parra H, Andersson E, Olsson H. A real-time thermal model of a permanent-magnet synchronous motor, Power Electronics. IEEE Trans 2010;25(2):463–74. <https://doi.org/10.1109/TPEL.2009.2027905>.
- [38] Li G, Ojeda J, Hoang E, Gabsi M, Lecrivain M. Thermal-electromagnetic analysis for driving cycles of embedded flux-switching permanent-magnet motors, Vehicular Technology. IEEE Trans 2012;61(1):140–51. <https://doi.org/10.1109/TVT.2011.2177283>.
- [39] Nerg J, Rilla M, Pyrhonen J. Thermal analysis of radial-flux electrical machines with a high power density, Industrial Electronics. IEEE Trans 2008;55(10): 3543–54. <https://doi.org/10.1109/TIE.2008.927403>.
- [40] Taylor GI. Distribution of velocity and temperature between concentric rotating cylinders. Proc Roy Soc Lond: Math. Phys. Eng. Sci. 1935;151(874): 494–512. <https://doi.org/10.1098/rspa.1935.0163>. <http://rspa.royalsocietypublishing.org/content/151/874/494.full.pdf>. <http://rspa.royalsocietypublishing.org/content/151/874/494>.
- [41] Gazley C. Heat transfer characteristics of rotational and axial flow between concentric cylinders. Trans. ASME 1958;80(1):79–90.
- [42] Becker KM, Kaye J. Measurements of diabatic flow in an annulus with an inner rotating cylinder. J Heat Tran 1962;84(2):97–104. <https://doi.org/10.1115/1.3684335>.
- [43] Zhang B, Qu R, Wang J, Xu W, Fan X, Chen Y. Thermal model of totally enclosed water-cooled permanent-magnet synchronous machines for electric vehicle application, Industry Applications. IEEE Trans 2015;51(4):3020–9. <https://doi.org/10.1109/TIA.2015.2409260>.
- [44] Ball bearings catalogue. 2013. accessed 2016-04-30, <http://www.skf.com/binary/138-121486/SKF-rolling-bearings-catalogue.pdf>.

- [45] Boglietti A, Cavagnino A. Analysis of the endwinding cooling effects in tefc induction motors, Industry Applications. IEEE Trans 2007;43(5):1214–22. <https://doi.org/10.1109/TIA.2007.904399>.
- [46] Grunditz EA. Design and assessment of battery electric vehicle powertrain, with respect to performance, energy consumption and electric motor thermal capability, Thesis for the degree of doctor of philosophy. Chalmers University of Technology; 2016. <http://publications.lib.chalmers.se/records/fulltext/236616/236616.pdf>.
- [47] Ball bearings. accessed 2016-03-30, <http://www.skf.com/group/products/bearings-units-housings/ball-bearings/index.html>; 2016.
- [48] M. D. Magnus Lindenmo, T. C. Support, No30 hi-lite material data, private Communication 2016-03-01.